Dry reforming of methane over embedded Ni nanoparticles in CeZrO2: Effect of Ce/Zr ratio and H2O addition

André L.A. Marinho, Raimundo Rabelo-Neto, Nicolas Bion, Fabio S Toniolo, Fabio B Noronha

To cite this version:

André L.A. Marinho, Raimundo Rabelo-Neto, Nicolas Bion, Fabio S Toniolo, Fabio B Noronha. Dry reforming of methane over embedded Ni nanoparticles in CeZrO2: Effect of Ce/Zr ratio and H2O addition. International Journal of Hydrogen Energy, 2024, 71, pp.1151-1163. ⟨10.1016/j.ijhydene.2024.05.337⟩. ⟨hal-04750184⟩

HAL Id: hal-04750184

https://hal.science/hal-04750184v1

Submitted on 23 Oct 2024

Dry Reforming of Methane over Embedded Ni nanoparticles in $CeZrO_2$: Effect of Ce/Zr ratio and H_2O addition

André L. A. Marinho [1,2,3], Raimundo C. Rabelo-Neto[2], Nicolas Bion [3], Fabio S. Toniolo [1], Fabio B. Noronha[2,4]*

[1] Federal University of Rio de Janeiro, Chemical Engineering Program of COPPE/UFRJ, P.O. Box 68502, CEP 21941-972, Rio de Janeiro, RJ, Brazil.

[2] National Institute of Technology, Catalysis Division, Rio de Janeiro, RJ 20081-312, Brazil.

[3] CNRS, University of Poitiers, Institut de Chimie des Milieux et Matériaux de Poitiers (IC2MP), TSA51106 – F86073 Poitiers Cedex 9, France

[4] University of Lille, CNRS, Centrale Lille, ENSCL, Univ. Artois, UMR 8181—UCCS—Unité de Catalyse et Chimie du Solide, 59000 Lille, France

* Corresponding author: fabio.bellot@int.gov.br

Submitted

to

International Journal of Hydrogen Energy

Abstract

Biogas has emerged as renewable source of CH_4 towards energy decarbonization in recent years. Among the biogas valorization routes, the dry reforming of methane (DRM) process is particularly interesting for H_2 production. However, the development of new catalysts with high metal dispersion and coke resistance is a significant challenge, particularly under industrial condition. Therefore, this work studies the performance of $Ni@Ce_xZr_{1-x}O_2$ catalysts with different Ce/Zr molar ratios for the dry reforming and bi-reforming of methane reactions. The addition of Zr promotes the Ni dispersion and the oxygen mobility of the support, leading to enhanced resistance to coke formation. Additionally, H_2O suppresses coke formation under high CH_4/CO_2 molar ratio, but catalyst deactivation is still observed. Finally, an optimal Ce/Zr molar ratio (i.e., 4.0) is achieved, demonstrating remarkable resistance to coke formation and high CH_4 and CO_2 conversion rates through the control of Ni particle size and the promotion of oxygen mobility.

Key words: Ni-embedded; Ceria; Ceria-Zirconia; Bi-reforming; Methane Dry Reforming; CO_2 reforming of CH_4; Biogas.

1. Introduction

The increase in global energy demand, associated with environmental issues and geopolitical aspects related to the availability of fossil fuels, has driven the development of new technologies for alternative fuel production, such as hydrogen [1]. Nowadays, the industrial production of hydrogen is extremely dependent on the availability of natural gas around the world, where around 80% of the hydrogen produced is from steam reforming of natural gas [2]. Therefore, there is an urgent need to develop sustainable production of H_2 using alternative feedstocks such as biogas.

Biogas is produced by the anaerobic digestion of biomass and is composed mainly of CH_4 and CO_2, whose composition varies depending on the feedstock [3]. Among the different processes for hydrogen production from biogas, the dry reforming of methane (DRM) reaction (Eq.1) is particularly attractive since CH_4 and CO_2 are already present in the biogas composition, and it has gained much more attention in recent years [4–6].

$$CH_4 + CO_2 \rightarrow 2CO + 2H_2 \qquad \Delta H^{\circ}_{298} = +\ 248\ \text{kJ/mol} \qquad (1)$$

The DRM is a highly endothermic reaction, and thus, it is performed at high temperatures (above 700°C) to achieve high conversion rates. Generally, Ni-based catalysts are used due to their high activity and low cost. However, under these severe reaction conditions, catalyst deactivation is an issue [4,7]. Catalyst deactivation may occur through three routes: (i) the sintering of Ni particles at high temperatures, decreasing the number of active sites for the reaction; (ii) the formation of coke through the decomposition of CH_4, leading to the blockage of active sites; and (iii) the oxidation of metallic Ni particles [8,9].

Some improvements in catalyst performance can be achieved by adjusting the operating conditions, such as the addition of steam to facilitate the bi-reforming reaction (BRM). A high steam-to-carbon ratio accelerates carbon gasification, reducing coke formation. However, the high cost of steam generation reduces the economic viability of the process [10]. Therefore, the development of the DRM process on a commercial scale is primarily focused on designing new Ni-based catalysts resistant to deactivation.

Redox supports have been extensively used to enhance catalyst stability. The high oxygen mobility of these supports contributes to carbon gasification, inhibiting coke accumulation on the catalyst surface. A two-step mechanism has been proposed to explain the DRM reaction, involving the occurrence of CH_4 decomposition on metal particles and CO_2 dissociation on oxygen vacancies of the support simultaneously [11–13]. Rabelo-Neto et al. [13] investigated the performance of Ni/SiCeO_2 catalysts for DRM. *In situ* XPS experiments showed a continuous change in ceria oxidation states between Ce^{4+} and Ce^{3+} under reaction conditions. This resulted in a high oxygen mobility of the ceria support, which reacts with carbon, inhibiting the formation of nickel carbide and consequently the nucleation and growth of carbon filaments. Vasiliades et al. [14] studied the effect of ceria morphology on the performance of Ni/CeO_2 catalysts for DRM. Ni supported on nanorod ceria exhibited a lower activation energy for bulk oxygen diffusion and higher oxygen supply to the surface than Ni/CeO_2 nanopolyhedra. Therefore, controlling CeO_2 morphology is responsible for promoting the carbon gasification rate and improving catalyst stability.

Another approach to increase the availability of oxygen vacancies in the catalyst is the use of metal dopants into CeO_2 structure through the formation of a solid solution [15–17]. Tu et al. [17] used a two-step hydrothermal process to synthesize Ni/$CeZrO_2$ (Ce/Zr = 1.0) catalyst with high oxygen storage capacity (OSC). As a result, the catalyst exhibited high coking tolerance during 16 hours of reaction at high CH_4 and CO_2 conversion rates (>80%).

In addition to the oxygen mobility in the support, special attention has been devoted to controlling Ni particle size during catalyst synthesis and the DRM reaction. It is well known in the literature that coke deposition originating from CH_4 decomposition is promoted over large Ni particles [18–20]. Vogt et al. [18] reported a structure sensitivity for the formation of carbon deposits over silica-supported Ni catalysts for DRM at 873 K. Increasing the Ni particle size from 1.2 to 6.0 nm increased the rate of carbon formation. They proposed that carbon formation occurs faster on the large particles containing highly coordinated sites. Da Fonseca et al. [19] controlled the rate of carbon formation over Ni/CeO_2 catalysts for DRM by tuning Ni crystallite size and oxygen vacancies of the support. The rate of carbon deposition increased as the Ni crystallite size increased, achieving a maximum at around 20-30 nm and then continuously decreased. However, carbon deposition was negligible below 10 nm and above 100 nm.

Therefore, several studies have been dedicated to design catalysts resistant to Ni sintering using different catalyst preparation methods such as the exsolution of metal nanoparticles from perovskites [21] and metal nanoparticles immobilized into mesoporous support [22]. More recently, the development of encapsulated catalysts has attracted more attention, as this unique structure (core-shell) combines the advantage of the confinement effect, isolating the Ni particles, with the high interaction between the active phase and the support [23–26]. Meng et al. [23] developed a Fe-Ni alloy material encapsulated into an SBA-15 mesoporous silica framework for the DRM reaction. This tailored material exhibits higher catalytic activity compared to Fe-Ni supported over amorphous SiO_2 due to the small Ni-Fe particle size within SBA-15 mesoporous, around 4 nm measured by TEM. Ni@SiO_2 catalysts with a core-shell structure were synthesized by the water-in-oil microemulsion method [25]. The Ni nanoparticles with diameters around 5 nm were obtained after hydrogen reduction at 750°C. The core-shell Ni@SiO_2 catalysts exhibited higher catalytic performance and stability for CO_2 reforming with methane reaction than the conventional supported Ni/SiO_2 catalysts, which were attributed to the confinement effect of the core-shell structure in limiting the sintering of Ni nanoparticles, the stronger metal-support interaction in stabilizing the catalyst structure, and the small Ni nanoparticles in minimizing the carbon deposition on the Ni@SiO_2 catalysts.

However, the preparation of core-shell catalysts is still challenging with several issues related to (i) the complexity of the preparation method involving several steps and expensive reactants; (ii) these methods lack reproducibility [27]. In our previous works [28–30], we developed an inexpensive method for the synthesis of Ni and Pt-based catalysts that produces metal nanoparticles embedded into ceria support. This is the so-called "sandwiched multi-core–shell structure”, which does not correspond to the typical core–shell material synthesis but the embedded structure has properties similar to them [27]. The carbon formation rate was significantly reduced for the Ni@CeO_2 catalyst and completely suppressed over the Ni@$Ce_{0.8}Zr_{0.2}O_2$ catalyst. The improved stability of the catalysts prepared by this method was attributed to the high resistance to sintering of the Ni nanoparticles embedded in the ceria and ceria-zirconia mixed oxide supports with high oxygen mobility.

In this work, the Ce/Zr molar ratio of Ni@$Ce_xZr_{1-x}O_2$ catalysts will be varied (Ce/Zr molar ratio = 4.0, 1.0, 0.25), and a relationship between the structure of embedded catalyst, ceria reducibility, oxygen mobility, and resistance to carbon formation with catalytic performance will be established. Despite the large number of papers dealing with the effect of Ce/Zr molar ratio on the performance of catalysts prepared by traditional methods, there are no works in the literature involving the embedded catalyst. Furthermore, the more stable catalyst was evaluated under different reaction conditions, such as CH_4/CO_2 molar ratio and steam addition in order to simulate the variation of such parameters as found in a real biogas stream.

2. Experimental

2.1. *Catalysts preparation*

The Ni@CeZrO_2 (X) catalysts, where X is the Ce/Zr molar ratio, were prepared by the sol-gel method described previously [30]. First, a solution of cerium nitrate (1.7 mol L^{-1}) was prepared, followed by the addition of an appropriate amount of nickel nitrate to obtain 10 wt% Ni in the catalyst. Then, a solution of zirconyl nitrate was added to prepare three different catalysts with Ce/Zr molar ratios equal to 4.0, 1.0, and 0.25. In another beaker, 25 mL of citric acid solution (6.7 mol L^{-1}) was prepared to obtain a citric acid/metals molar ratio equal to 1.0. Finally, both solutions were mixed and stirred for 2 hours at room temperature to promote gel formation. The solution was then heated at 70 °C under vacuum to remove water and dried at 100 °C overnight in an oven. Calcination occurred in two steps using a heating rate of 1 °C/min: (i) from 25 to 300 °C, maintained at this temperature for 2 hours; (ii) from 300 °C up to 400 °C, maintained for 4 hours. The catalysts were denominated as Ni@CeZrO_2 (4), Ni@CeZrO_2 (1), and Ni@CeZrO_2 (0.25).

2.2. *Catalysts characterization*

2.2.1. X-ray fluorescence (XRF)

The amount of Ni and the Ce/Zr molar ratio in the catalysts were determined by X-ray fluorescence spectroscopy, using a RIGAKU RIX-3100 spectrometer.

2.2.2. N_2 physisorption

The specific surface area of the reduced samples was measured by N_2 adsorption adopting the Brunauer, Emmett and Teller (BET) model. Firstly, the samples were treated under pure hydrogen (30 mL min^{-1}) from 25 up to 800 °C, simulating the temperature reaction. The analysis was performed in a Micromeritics Tristar 3000 apparatus at – 196 °C. The samples were previously degassed at 300 °C under vacuum for total cleaning of the surface.

2.2.3. X-ray diffraction (XRD)

In situ X-ray diffraction was performed in a Bruker D8 Advance X-ray powder diffractometer operated at 40 kV and 40 mA, using CoKα radiation (λ = 1.7903 Å), equipped with a Position Sensitive Detector, VANTEC-1, kβ filter (Ni), used in scanning mode. The 2θ range analyzed was 10 to 80°, step of 0.05°, step time equal to 2 s. The samples were reduced under a flow of 10 % H_2/He mixture and the XRD patterns were collected at different temperatures (room temperature, 300 °C, 500 °C, 800 °C). The average crystallite size of CeO_2 was calculated using the Scherrer's equation (Eq. 1), considering the width at half maximum value obtained in the most intense line of CeO_2 ($2\theta = 28.6^o$), k = 0.9 (spheric particles) and λ = 0.1540 nm (CuKα X-ray source). The CeO_2 lattice parameter was determined using equation 2.

$$\mathrm{d} = \frac{\mathrm{k} \,.\, \lambda}{\beta \,.\, \cos\theta} \tag{1}$$

$$a = \sqrt{d^2 \,.\, (h^2 + k^2 + l^2)} \tag{2}$$

Ex situ X-ray diffraction was performed in a RIGAKU diffractometer using CuKα radiation (λ = 1.5406 Å). The calcined samples were previously reduced with pure hydrogen (30 mL min^{-1}) at 800 °C for 1h, followed by purge with N_2 (30 mL min^{-1}) during 30 min at the same temperature. Then, the reactor was cooled down to room temperature and immersed in an isopropyl alcohol/liquid nitrogen bath to decrease the temperature to -65 °C. At this temperature, the catalyst was passivated with a 5% O_2/N_2 mixture during 1h. The patterns were collected over the range 10° to 90° using a scan rate of 0.02°/step and 1 s/step. The Scherrer equation was used to estimate the Ni^0 crystallite size.

2.2.4. Raman spectroscopy

The samples were analyzed in a Raman Horiba Jobin Yvon spectrometer using a He:Ne laser (632 nm).

2.2.5. Transmission electron microscopy (TEM)

TEM analysis of Ni@CeZrO$_2$ (4) reduced catalyst was performed in a JEOL 2100 UHR apparatus at 20 keV, with 0.19 and 0.14 nm punctual and linear resolution, respectively, equipped with a LaB6 filament. Before the analysis, the sample was reduced at 800 °C for 1 h, the same temperature used for the reaction.

2.2.6. $^{18}O_2$/$^{16}O_2$ isotopic exchange

The experiments were conducted using a closed recycling system that was connected to a Pfeiffer Vacuum quadrupole mass spectrometer and a vacuum pump. Initially, the sample (20 mg) was treated with a flow of $^{16}O_2$ (50 mL min^{-1}, 500 °C, 1 h) and evacuated for 1 h. The sample was then cooled to the desired exchange temperature (400 °C).

For the Isothermal Oxygen Isotopic Exchange (IOIE) experiment, the exchange was carried out at 400 °C. 55 mbar of pure $^{18}O_2$ gas (≥ 99 at.%, ISOTEC) was introduced into the reactor, and the concentration of each isotopomer was monitored by observing the m/z signals of 32 ($^{16}O_2$), 34 ($^{18}O^{16}O$), and 36 ($^{18}O_2$).

To calculate the atomic fraction of $^{18}O_2$ in the gas phase at time t (α_g^t) (Eq. 3) and the number of oxygen atoms exchanged (Ne) (Eq. 4), the following equations were used:

$$\alpha_g^t = \frac{1/2\, P_{34}^t + P_{36}^t}{P_{32}^t + P_{34}^t + P_{36}^t} \quad (3)$$

$$N_e = \left(\alpha_g^0 - \alpha_g^t\right) N_g \, \frac{1}{w} \quad (4)$$

Where Ng represents the total number of oxygen atoms in the gas phase, w represents the weight of the catalyst, and α_g^0 represents the initial atomic fraction of $^{18}O_2$ in the gas phase.

2.2.7. Thermogravimetric analysis (TG)

To measure the amount of coke that was deposited on the catalyst during reaction, spent catalysts were subjected to thermogravimetric analyses using a TA Instruments equipment (SDT Q600). The catalyst sample was cooled from reaction temperature up to 25 °C under N_2 atmosphere in order to avoid carbon oxidation. Then, 10 mg of the spent catalyst was placed in the equipment and heated in synthetic air flow (100 mL min^{-1}) from room temperature to 1000 °C, while the weight change was recorded, at a heating rate of 20 °C/min.

2.2.8. Scanning electron microscopy (SEM)

SEM analyses of the spent catalysts were carried out using a field emission scanning electron microscope (FE-SEM) Quanta FEG 450 FEI operating with an accelerating voltage of 20 kV.

2.3. Catalytic tests

The DRM and BRM catalytic tests were performed with the same amount of catalyst and pre-treatment. The samples were diluted with SiC (SiC mass/catalyst mass ratio = 1.5) to avoid hot spot formation or temperature gradients. Different catalyst mass was used in order to obtain approximately the same initial conversion for all Ce/Zr molar ratio. The catalysts were reduced under pure H_2 (30 mL min^{-1}) at 800 °C (10 °C min^{-1}) for 1 h and purged under N_2 at the same temperature for 30 min.

The DRM catalytic tests were performed in a fixed-bed reactor at atmospheric pressure. A reactant mixture with various CH_4:CO_2 molar ratios (0.67; 1.00; 1.50) under flow rate of 100 mL min^{-1} was used for the DRM at 800 ºC. The reaction products were analyzed by gas chromatography (Agilent 6890) equipped with a thermal conductivity detector and Carboxen 1010 column (Supelco).

To perform the BRM reaction, a U-shaped quartz reactor was used at 800 °C and atmospheric pressure for 24 hours. Prior to the reaction, the catalyst was reduced under pure H_2 at 800 °C (30 mL min^{-1}, 10 °C min^{-1}) for 1 hour, then kept at this temperature for 30 minutes under He. To obtain the reactant mixture $CH_4/CO_2/H_2O$, a CH_4 stream (50 mL/min) passed through a saturator containing water (76 °C) and then CO_2 stream (33 mL/min) was added to the CH_4/H_2O mixture. The resulting mixture contained 43% CH_4, 28.5% water, and 28.5% CO_2. The reaction products were analyzed in a similar equipment previously described. The CH_4 and CO_2 conversion were determined as follow:

$$X_{CH_4} = \frac{(n_{CH_4})_{feed} - (n_{CH_4})_{exit}}{(n_{CH_4})_{feed}} \text{ x } 100 \qquad (5)$$

$$X_{CO_2} = \frac{(n_{CO_2})_{feed} - (n_{CO_2})_{exit}}{(n_{CO_2})_{feed}} \text{ x } 100 \qquad (6)$$

3. Results and discussion

3.1. *Catalyst characterization*

The chemical composition and BET surface area of the samples after reduction at 800 °C under pure H_2 are listed in Table 1. The Ni content and Ce/Zr molar ratio are close to the nominal values. All catalysts exhibited a very low surface area due to the sintering of CeO_2 at high reduction temperature [31].

Table 1. Chemical composition and BET surface area after reduction of the catalysts at 800 °C.

Catalyst	Ni (wt%)	CeO_2 (wt%)	Dopant (wt%)	Ce/Dopant molar ratio	BET surface area of reduced samples (m^2/g)
Ni@CeZrO$_2$(4.0)	9.5	74.4	13.4	4.0	21
Ni@CeZrO$_2$ (1)	11.1	47.8	38.0	0.9	11
Ni@CeZrO$_2$ (0.25)	10.7	21.4	65.0	0.24	16

Fig. 1 shows the Raman spectra of the calcined samples. The spectrum of CeO_2 is included for comparison. The CeO_2 spectrum exhibits an intense band at 462 cm^{-1}, which is assigned to the symmetrical stretching mode between the eight oxygen atoms bound to the cerium atom in the triple degenerate F_{2g} mode. For Ni@$CeZrO_2$ (4) and Ni@$CeZrO_2$ (1), the addition of zirconia causes a shift in this band toward higher wavenumbers. Due to the smaller ionic radius of Zr^{4+} (0.84 Å) compared to Ce^{4+} (0.97 Å) [32], the introduction of zirconium into ceria's framework results in the contraction of its structure, which can be noticed by the shift of the band located at 462 cm^{-1} [15,33,34]. Furthermore, there is also the appearance of a broad band between 500 – 650 cm^{-1}. According to the literature, two broad bands appear with the solid solution formation: one around 570 – 590 cm^{-1} and the other located between 610 - 640 cm^{-1}. Both bands are related to the generation of oxygen vacancies. The first region is attributed to the extrinsic vacancies, which correspond to oxygen vacancies generated by the substitution of Ce^{4+} by Zr^{4+}; whereas the second represents the intrinsic vacancies formed by the appearance of Ce^{3+} ions into ceria's structure [35,36]. Further increase in the Zr content produces significant changes in the spectrum of Ni@$CeZrO_2$ (0.25) catalyst, with bands characteristic of zirconia with a tetragonal structure [34,37].

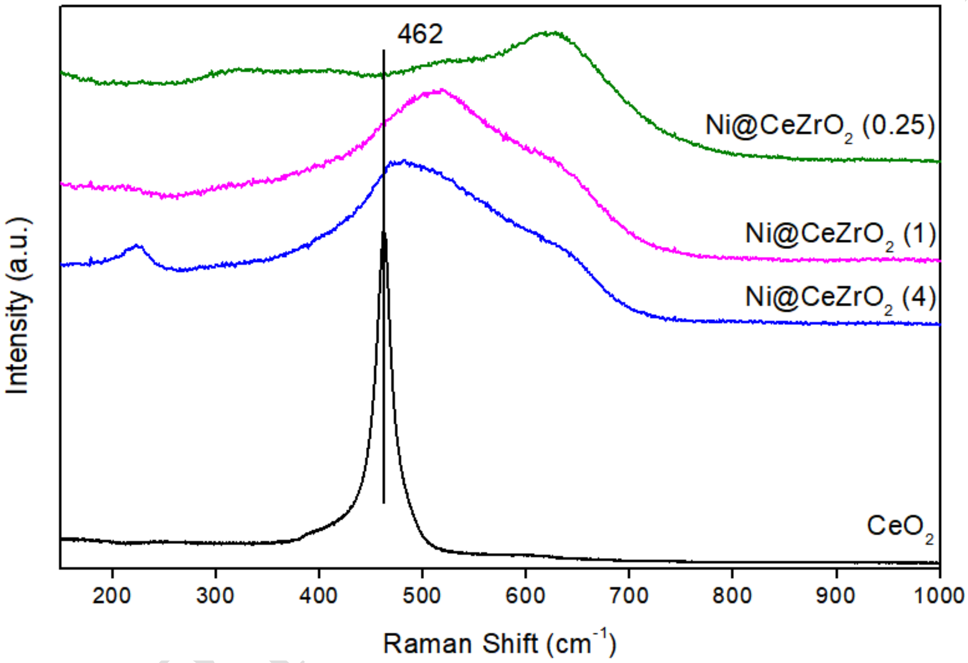

Figure 1. Raman spectra for the calcined samples and CeO_2 reference.

Fig. 2 shows the diffractograms of the calcined samples. The XRD patterns have been converted to CuKα radiation for comparison with literature, and the peak at 44.5° is attributed to the Khantal material used on the sample holder of the XRD instrument. The characteristic lines of CeO_2 with a fluorite-like structure (JCPDS 34-0394) are marked with dashed lines for better understanding of the shifts observed with the addition of dopants.

The insertion of Zr shifts the lines of CeO_2 to higher 2θ values due to the formation of a ceria-zirconia solid solution [32]. This result agrees very well with the experiments of Raman spectroscopy. The calculated ceria lattice value for the calcined samples is: Ni@CeO_2 (5.4189 Å); Ni@$CeZrO_2$ (4.0) (5.3615 Å); Ni@$CeZrO_2$ (1.0) (5.2822 Å). The addition of high Zr content (Ce/Zr = 0.25) leads to the formation of an amorphous $CeZrO_2$ structure, resulting in a broad peak centered at 31.6°. For this reason, the peak is not very well defined to determine the ceria lattice. The increase in the Zr content creates geometric and compositional disorders in the material structure, decreasing its crystallinity.

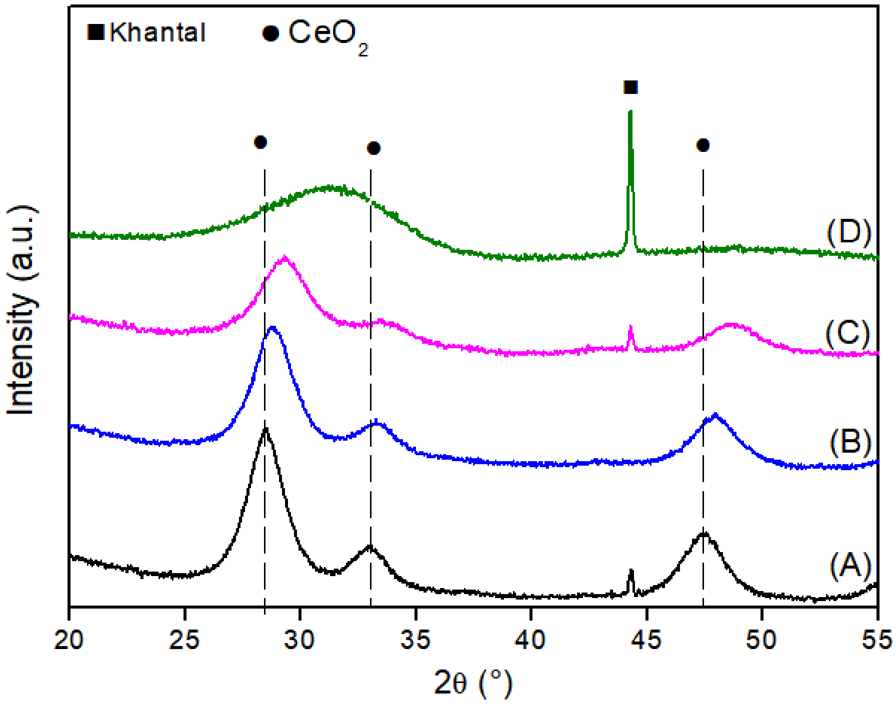

Figure 2. XRD patterns of the (A) Ni@CeO_2, (B) Ni@$CeZrO_4$ (4), (C) Ni@$CeZrO_2$ (1) and (D) Ni@$CeZrO_2$ (0.25) calcined samples.

Teles et al. [34] prepared Pd/$Ce_xZr_{1-x}O_2$ catalysts with different Ce/Zr molar ratios and obtained catalysts with high crystallinity and different structures depending on the Ce/Zr molar ratio used: the formation of a cubic structure with Ce/Zr molar ratio higher than 1.0 and a tetragonal structure below 1.0. Unlike our work, the authors prepared the support using the co-precipitation method, highlighting the synthesis effect on the crystallinity of $CeZrO_2$ at high Zr content in the support. Therefore, in our work, XRD of the fresh samples shows that Zr^{4+} partially replaces Ce^{4+} in the structure, leading to the formation of $CeZrO_2$ solid solutions [38]. The characteristic lines of NiO were not detected in the diffractograms of the calcined samples, indicating the presence of highly dispersed nanoparticles.

The diffractograms obtained during the *in situ* reduction of the samples are shown in Fig. 3. For Ni@$CeZrO_2$ (4) and Ni@$CeZrO_2$ (1) catalysts, the main ceria line around $2\theta = 28°$ shifts to lower angles when the samples are heated to 500 °C under H_2 atmosphere, and this displacement is more pronounced at 800 °C. However, this shift is only observed after reduction at 800 °C for Ni@CeO_2. This shift is caused by the expansion of the ceria structure due to two phenomena: (i) thermal expansion of the unit cell; (ii) reduction of Ce^{4+} to Ce^{3+}, which has a larger ionic radius (1.14 Å) [39]. Therefore, the displacement observed during the experiment is the sum of both effects and is more pronounced for Ni@$CeZrO_2$ (4) and Ni@$CeZrO_2$ (1) catalysts due to the presence of a solid solution. The Ni@$CeZrO_2$ (0.25) only presented a crystalline phase at 800 °C ascribed to the $CeZrO_2$ solid solution with a tetragonal structure, as observed previously in the literature for the $CeZrO_2$ system with high Zr content [34].

The ceria lattice parameter increases for both Zr-doped catalysts during heating up to 800 °C (Fig. 4 A), and this variation is higher than that observed for Ni@CeO_2, following the order: Ni@CeO_2 (0.0924 Å) < Ni@$CeZrO_2$ (1) (0.0976 Å) < Ni@$CeZrO_2$ (4) (0.1011 Å). Our previous publication [30] has shown that the variation of the ceria lattice parameter due to thermal expansion is only 0.04 Å, but the catalysts exhibited higher variations in the present work, indicating ceria reduction. Therefore, doping with Zr for the catalysts with a Ce/Zr ratio of 4 and 1 enhances ceria reduction, improving the creation of oxygen vacancies in the material. Prasad et al. [40] demonstrated by DFT studies that the oxygen vacancy formation energy decreased by the incorporation of Zr^{4+} into the ceria structure and enhanced the mobility of O anions.

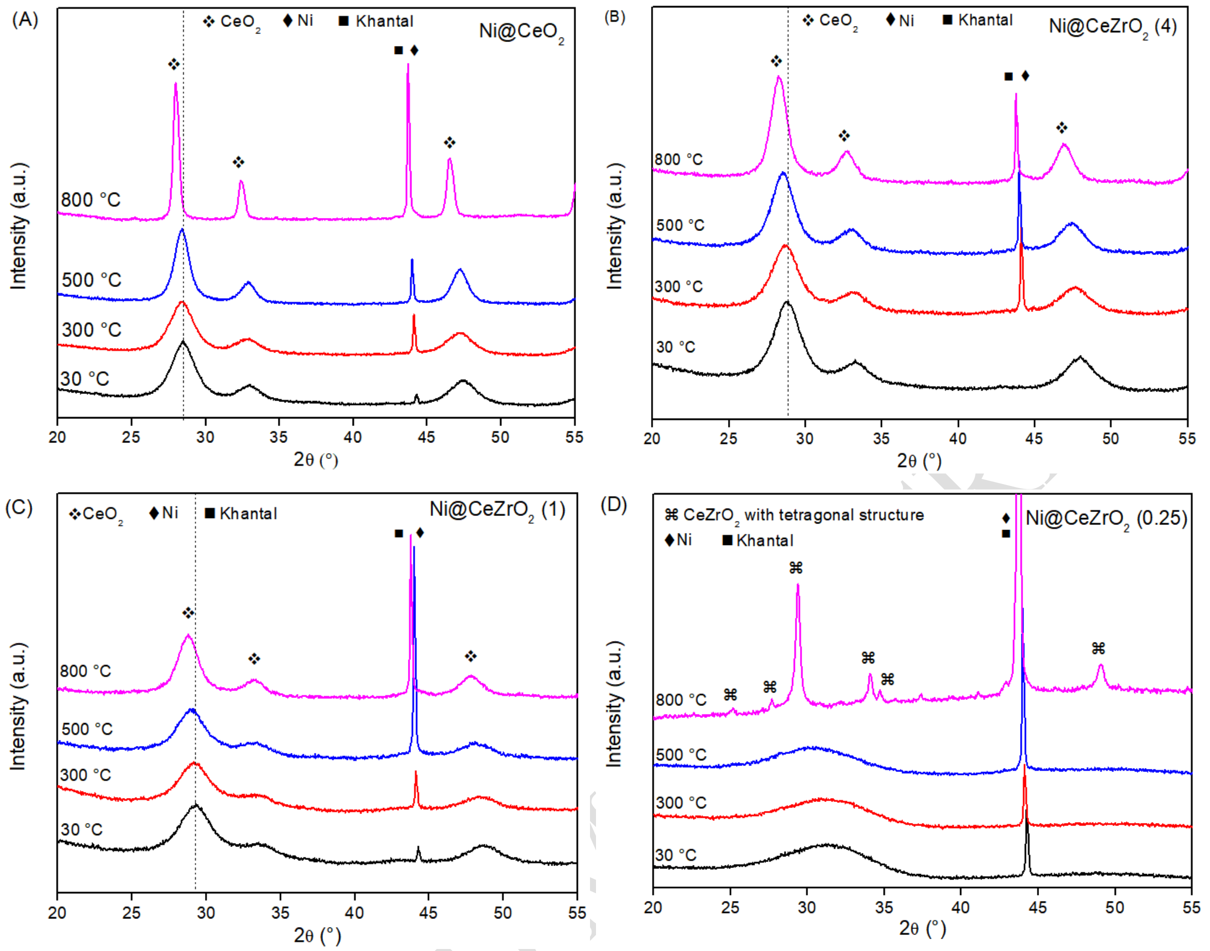

Figure 3. Effect of Ce/Zr molar ratio in the CeZrO$_2$ solid solution structure during *in-situ* reduction followed by XRD for (A) Ni@CeO$_2$, (B) Ni@CeZrO$_2$ (4), (C) Ni@CeZrO$_2$ (1) and (D) Ni@CeZrO$_2$ (0.25) catalysts.

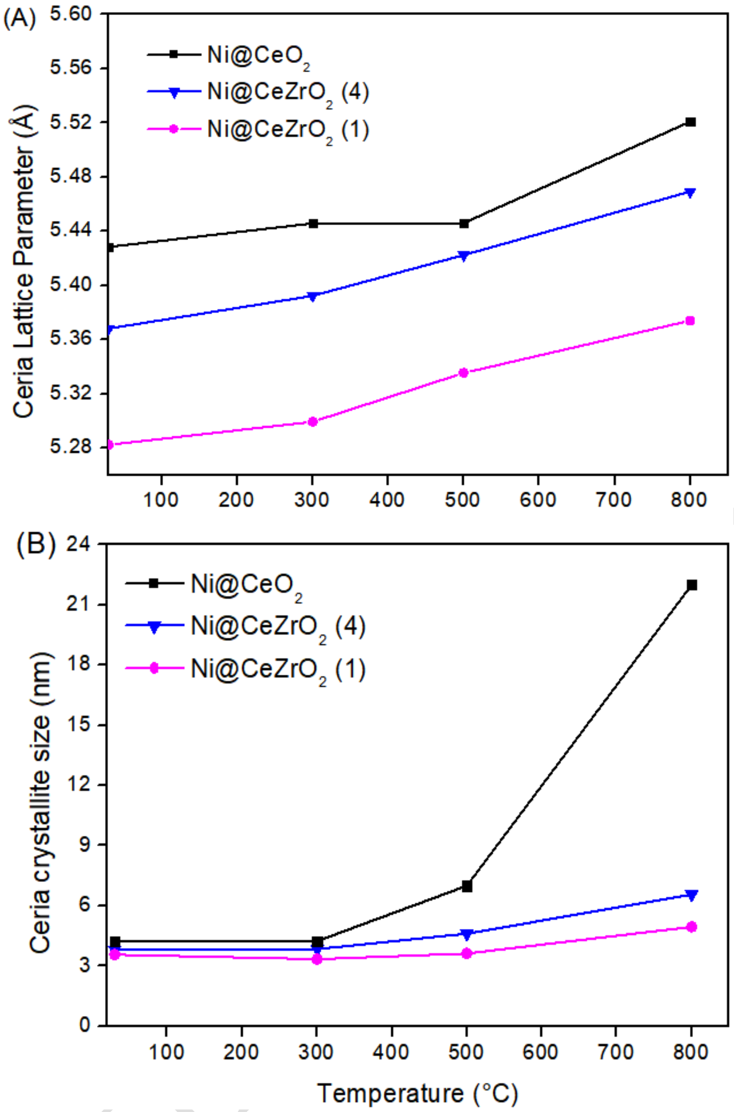

Figure 4. Variation of (A) ceria lattice parameter and (B) ceria crystallite size during reduction process.

Moreover, as seen in Fig. 4B, the Zr-doped catalysts exhibit high thermal stability, preventing the sintering of CeO_2 particles at high temperatures. The Ni@CeO_2 catalyst has the largest ceria crystallite size (22 nm) at 800 °C, while Ni@$CeZrO_2$ (4) and Ni@$CeZrO_2$ (1) have sizes of 6.6 nm and 5.0 nm, respectively. The amorphous structure of Ni@$CeZrO_2$ (0.25) indicates the formation of smaller particles. These results highlight the high resistance to CeO_2 sintering due to the formation of a $CeZrO_2$ solid solution [33].

The Ni crystallite size during *in situ* reduction could not be determined due to equipment limitations (overlap of metallic Ni and equipment lines). Therefore, the Ni crystallite size was calculated by XRD using *ex situ* reduced samples at 800 °C followed by passivation (Fig. 5, Table 2). All Ni/$CeZrO_2$ catalysts exhibited small Ni nanoparticles (< 5.5 nm) compared to those synthesized by classical impregnation [30]. The Ni crystallite size followed the order: Ni@CeO_2 > Ni@$CeZrO_2$ (4) > Ni@$CeZrO_2$ (1) > Ni@$CeZrO_2$ (0.25). Unlike more conventional methods, the sol-gel technique allows for the preparation of catalytic materials in a "one-pot" process with a homogeneous distribution of components on the atomic scale at low-temperature synthesis and cost. The sol-gel technique enables the control of composition, homogeneity, and structural properties of solids, promoting catalytic properties such as oxygen vacancies and metal-support interaction [41,42].

To confirm the XRD results, TEM analysis was performed on the Ni@$CeZrO_2$ (4) reduced catalyst (Fig. S1). The image of the catalyst reveals the presence of small Ni nanoparticles embedded in the ceria-zirconia matrix with sizes around 6 nm, similar to the value obtained by the Scherrer's equation (5.4 nm). Therefore, the embedded structure prevents Ni sintering at high reduction temperatures. Moreover, the thermal stability due to the $CeZrO_2$ solid solution also contributes to Ni stabilization.

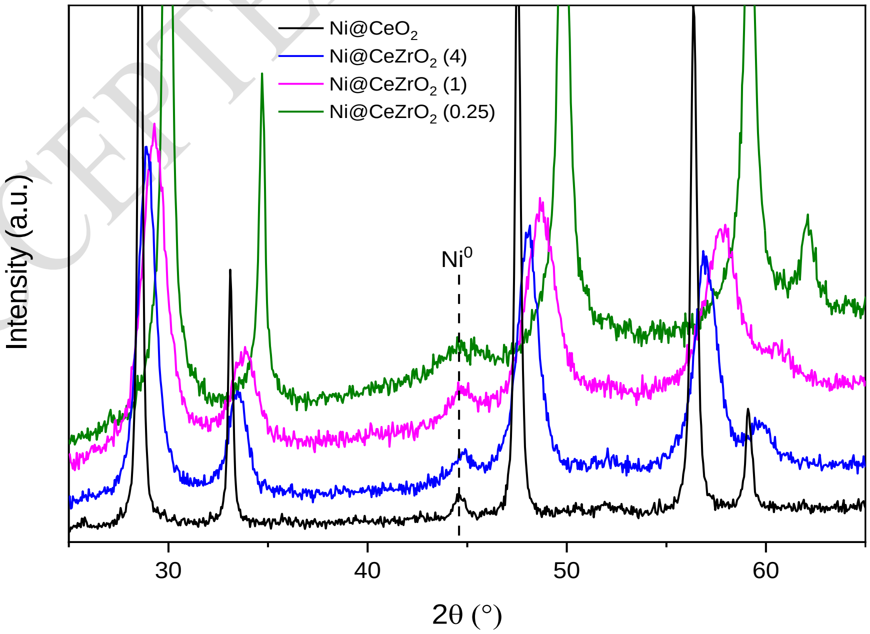

Figure 5. XRD results of catalysts after *ex-situ* reduction and passivation.

Table 2. Ni crystallite size of the samples reduced at 800 °C and passivated at room temperature.

Catalyst	Ni crystallite size (nm)
Ni@CeO$_2$	10.7
Ni@CeZrO$_2$ (4)	5.4
Ni@CeZrO$_2$ (1)	3.0
Ni@CeZrO$_2$ (0.25)	2.0

The oxygen mobility of each catalyst was measured by IOIE experiments, and the number of exchanged oxygen atoms (N$_e$) as a function of time at 400 °C is presented in Fig. 6. By monitoring the gas composition using mass spectrometry, it is possible to quantify the evolution of the amount of ^{16}O atoms released by the catalyst exchanging with the gas phase rich in ^{18}O2. The Ni@CeZrO$_2$ (4) catalyst exhibits the highest initial rate of exchange (Table 3), as observed by the curve inclination of N$_e$ vs. time, reaching the value of N$_e$ = 39 x 10^{20} at g^{-1} exchanged after 90 minutes of the experiment, followed by the Ni@CeZrO$_2$ (1) (N$_e$ = 33 x 10^{20} at g^{-1}) and Ni@CeZrO$_2$ (0.25) (Ne = 26 x 10^{20} at g^{-1}).

Similar results were obtained in the literature for CeZrO$_2$ materials [43,44], which were attributed to the low oxygen storage capacity of the Zr-rich solid solutions since the oxygen atoms linked to Zr are not exchangeable [45]. According to the literature [46], the performance of ceria-based solid solutions in the DRM reaction and the redox behavior are significantly influenced by their composition and morphology, where the enhanced amount of oxygen vacancies and their reactivity play a key role in the redox characteristics and catalytic performance of the catalysts. Vasiliades et al. [14] performed ^{16}O/^{18}O transient isothermal isotopic exchange experiments over Ni/CeO$_2$ material with different ceria morphologies. In their work, they correlated the enhanced oxygen exchange capacity in Ni/CeO$_2$ nanorods with the low activation energy for carbon oxidation by lattice oxygen species, providing promoted DRM performance. Our previous work [30] has shown that the addition of Zr into the ceria structure increases the value of N_e exchanged in comparison to the Ni@CeO$_2$ catalyst due to the participation of oxygen species from the bulk phase. Herein, the results show that the Ce/Zr molar ratio strongly affects the oxygen mobility of the materials; further increase in the Zr content reduces the amount of oxygen mobility and the rate of oxygen exchange. Thus, the IOIE experiments show that the highest oxygen mobility is observed for the Ni@CeZrO$_2$ (4) catalyst.

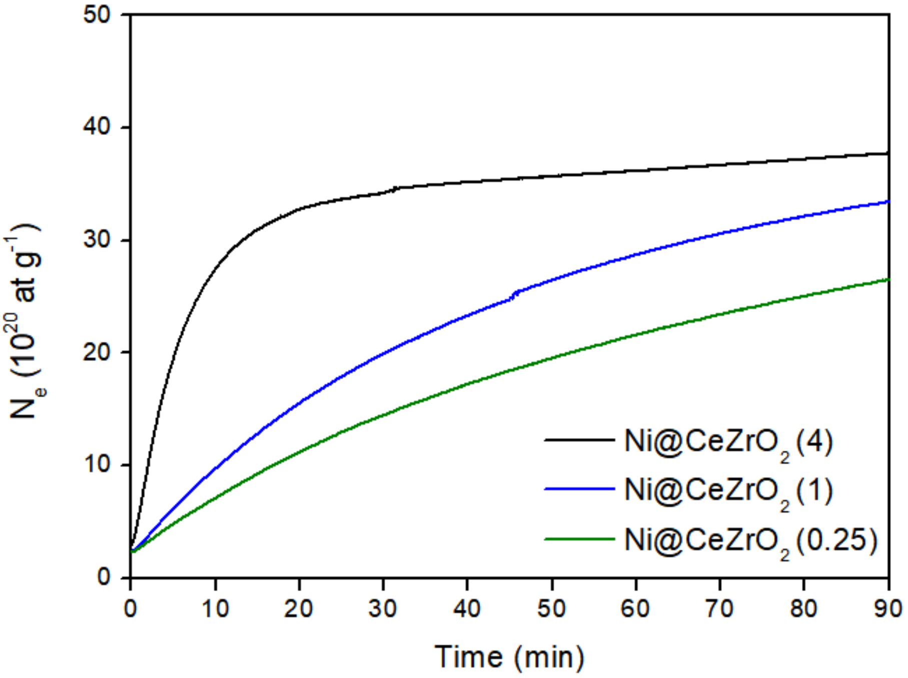

Figure 6. IOIE experiments of the Ni@CeZrO$_2$ catalysts at 400 °C.

Table 3. Initial rate of oxygen exchange at 400 °C.

Catalyst	**Initial Rate of Exchange (10^{20} at g^{-1} min^{-1})**
Ni@CeZrO$_2$ (4)	3.8
Ni@CeZrO$_2$ (1)	0.8
Ni@CeZrO$_2$ (0.25)	0.5

3.2. *DRM reaction: Effect of CH_4/CO_2 molar ratio*

Fig. 7 shows the evolution of CH_4 and CO_2 conversions as well as the H_2/CO molar ratio as a function of time on stream (TOS) at 800 °C and $CH_4/CO_2 = 1.0$. The gas hourly space velocity (GHSV) was reduced for the Ni@CeZrO2 (1) and Ni@CeZrO2 (0.25) catalysts to obtain similar initial CH_4 conversion, as they were less active compared to the Ni@$CeZrO_2$ (4) catalyst. A similar trend was observed in the literature where the $CeZrO_2$ solid solution with a Ce/Zr molar ratio lower than 4.0 also presented a decrease in their activity, but the authors did not provide any explanation [47,48].

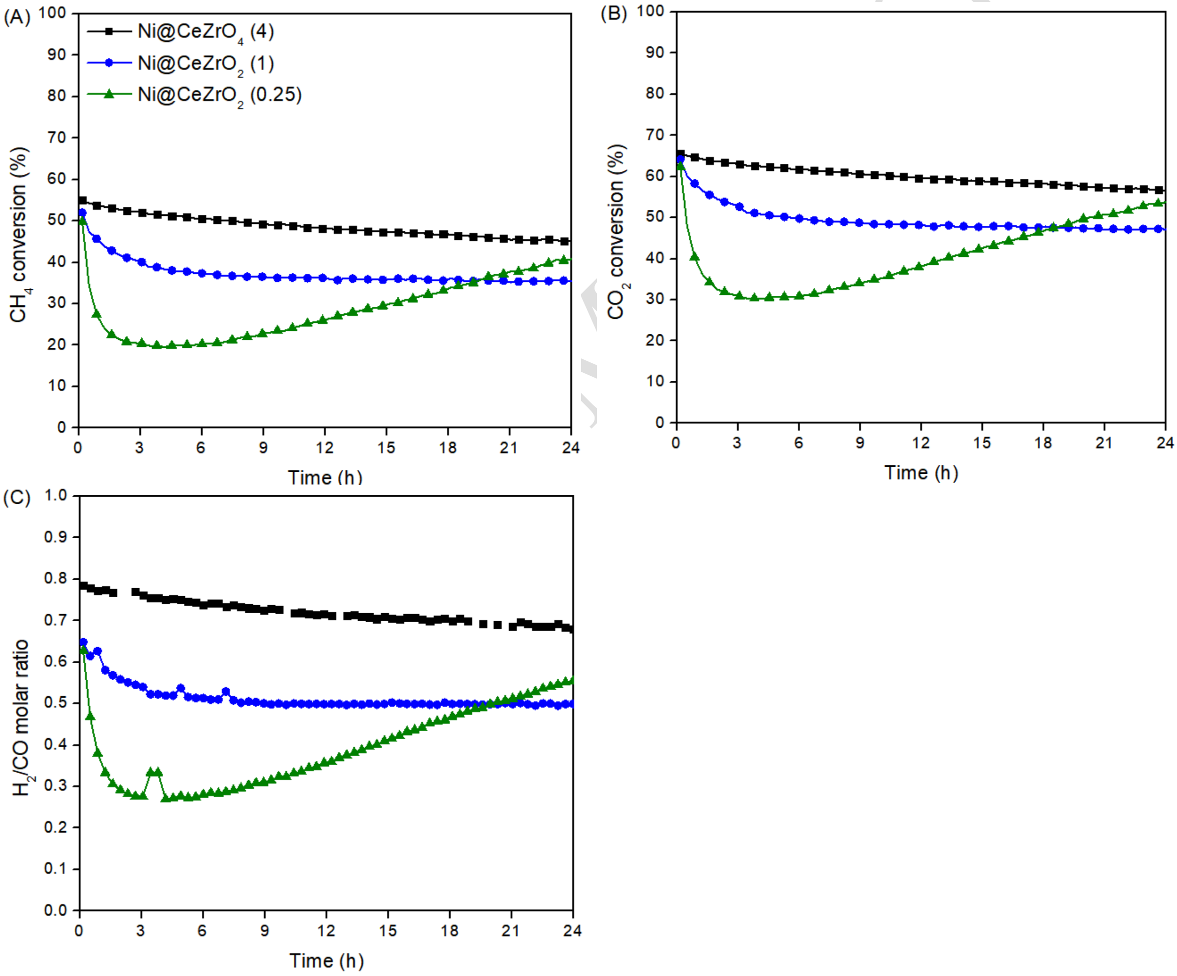

Figure 7. (A) CH_4 Conversion, (B) CO_2 conversion and (C) H_2/CO molar ratio obtained as a function of TOS for Ni@$CeZrO_2$ (4) (GHSV = 300 L g_{cat}^{-1} h^{-1}), Ni@$CeZrO_2$ (1) (GHSV = 86 L g_{cat}^{-1} h^{-1}) and Ni@$CeZrO_2$ (0.25) (GHSV = 43 L g_{cat}^{-1} h^{-1}) catalysts. Reaction condition: $CH_4/CO_2 = 1.0$, T = 800 °C and P = 1 bar.

The catalysts exhibit high conversion of CH_4 and CO_2, confirming the accessibility of reactants to the Ni nanoparticles formed within the $CeZrO_2$ support. The Ni@$CeZrO_2$ (4) catalyst is quite stable during 24 hours of TOS, producing syngas with an H_2/CO molar ratio around 0.8. The CO_2 conversion was higher than the CH_4 conversion due to the occurrence of the reverse water-gas shift (RWGS) reaction, as previously reported in the literature [19], leading to the production of CO and H_2O and consequently, a H_2/CO ratio lower than 1.0. However, Ni@$CeZrO_2$ (1) and Ni@$CeZrO_2$ (0.25) catalysts showed a decrease in the CH_4 and CO_2 conversions at the beginning of the reaction, followed by a reduction in the H_2/CO molar ratio. After 5 hours of reaction, the Ni@$CeZrO_2$ (1) catalyst becomes quite stable, whereas the Ni@$CeZrO_2$ (0.25) catalyst undergoes an activation process, followed by an increase in the H_2/CO molar ratio.

The initial deactivation observed for Ni@$CeZrO_2$ (1.0) and Ni@$CeZrO_2$ (0.25) catalysts could be associated with the carbon formation. However, DTG curves did not show the presence of carbon deposits in the post-reaction samples probably due to the redox mechanism of $CeZrO_2$ support and the high Ni dispersion (Fig. 8A and Fig. S2).

The design of catalysts with small Ni nanoparticles has proven to be an efficient approach to avoid coke formation [49]. Recently, Li et al. [50] developed a Ni/CeO_2 catalyst where the Ni nanoparticles are confined within the honeycomb-lantern-like structure of CeO_2. They observed an increase in the catalyst activity and stability compared to other CeO_2 structures (spheres or bulk particles), which was associated with the spatial confinement responsible for enhancing the Ni thermal stability. Also, the promotion of metal/support interfaces contributes to decreasing the energy barrier for the DRM reaction.

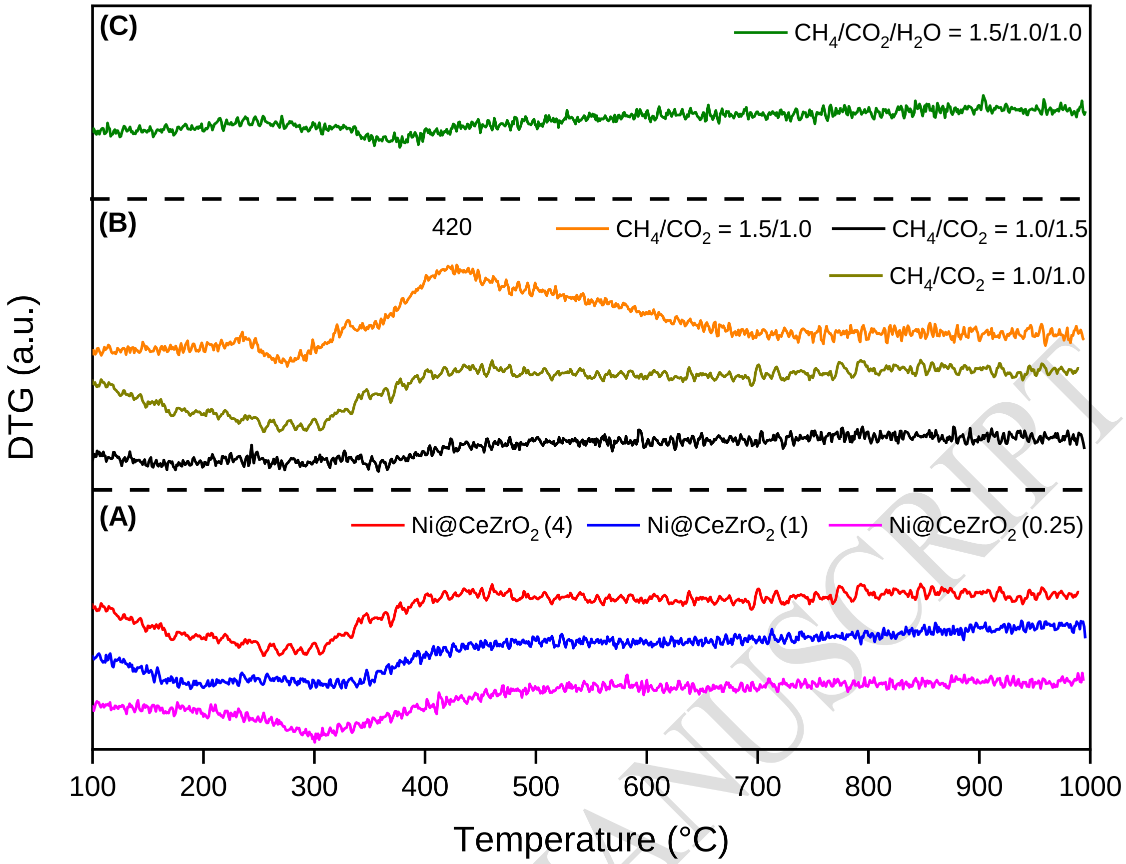

Figure 8. DTG curves of the post-reaction samples after reaction under different conditions in this work: (A) Variation of Ce/Zr molar ratio in the DRM reaction with CH_4/CO_2 = 1.0/1.0; (B) Effect of CH_4/CO_2 molar ratio in the DRM performance of Ni@$CeZrO_2$ (4) catalyst; (C) Effect of water addition in the DRM performance of Ni@$CeZrO_2$ (4) catalyst.

In our work, the higher interaction between Ni and the support inhibits the detachment of Ni particles from $CeZrO_2$ and the growth of carbon filament, suppressing carbon deposits over the catalyst and the agglomeration of Ni nanoparticles. In fact, SEM images (Fig. 9) of the post-reaction catalysts did not show any carbon filaments after 24 hours, in accordance with the TGA-DTG results (Fig. 8A).

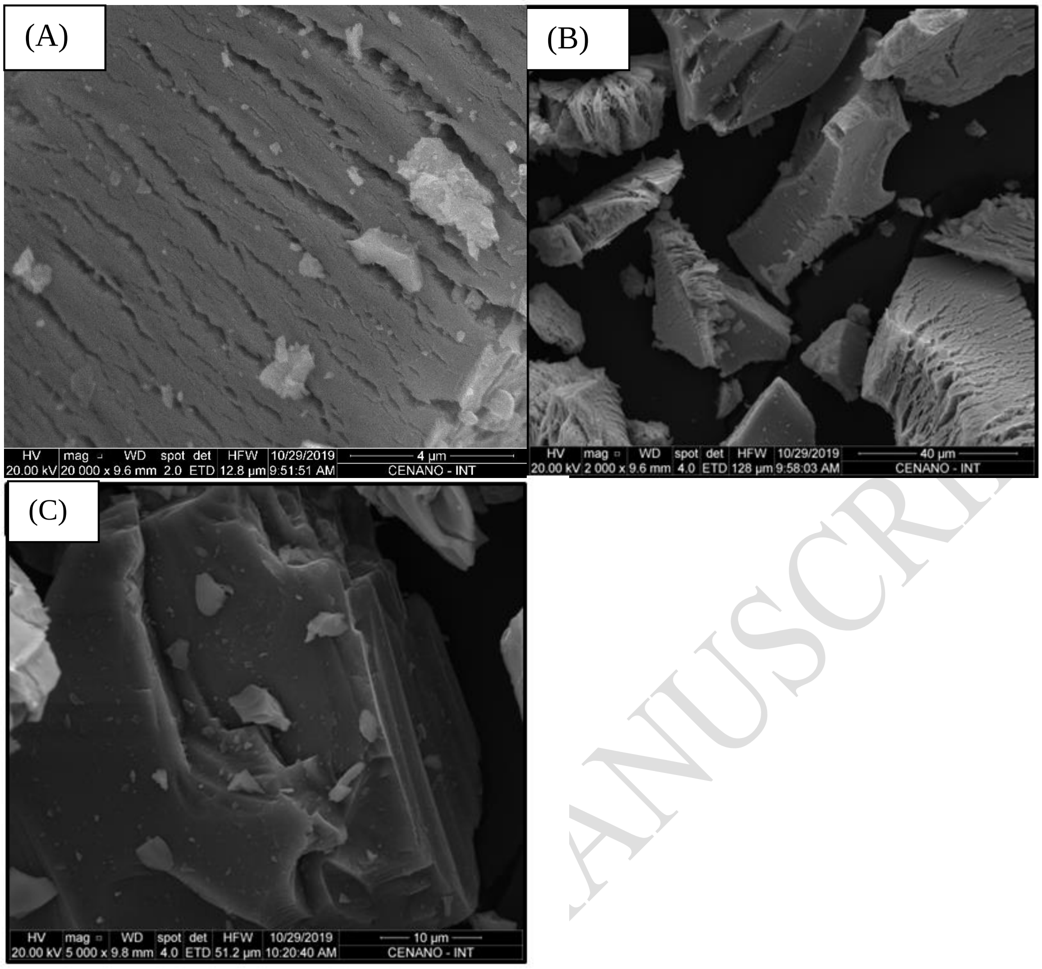

Figure 9. SEM images of the (A) Ni@CeZrO$_2$ (4), (B) Ni@CeZrO$_2$ (1) and (C) Ni@CeZrO$_2$ (0.25) spent catalysts after DRM reaction with CH$_4$/CO$_2$ = 1.0/1.0.

Therefore, the deactivation observed for the Ni@CeZrO$_2$ (1) and Ni@CeZrO$_2$ (0.25) catalysts is not due to carbon deposition. The performance of Ni/CeZrO$_2$ catalysts in this work is compared with the literature data in Table 4. Despite the large number of papers dealing with Ni/CeO$_2$ catalysts prepared by different techniques for DRM reaction, the development of such catalyst resistant to coke formation is still a challenge for this reaction, as shown in Table 4. In comparison to the literature, the embedded Ni nanoparticles in CeZrO$_2$ developed in our work are promising catalysts for the DRM concerning carbon resistance.

Table 4. Catalyst performance during the DRM reaction (catalyst structure, activity and resistance to carbon formation) compared with literature data.

Catalyst	Catalyst Structure	Stability Test	Carbon formation rate (mgC.g_{cat}^{-1}.h^{-1})	Reference
Ni@CeO_2 (4)	Ni embedded into support	GHSV = 300 L.g_{cat}^{-1}.h^{-1} T = 800 °C; P = 1 bar; CH_4/CO_2 = 1.0 Initial XCH_4 = 55 % Initial XCO_2 = 66 % t = 24h	No carbon formation	This work
Ni@CeO_2 (1)	Ni embedded into support	GHSV = 86 L.g_{cat}^{-1}.h^{-1} T = 800 °C; P = 1 bar; CH_4/CO_2 = 1.0 Initial XCH_4 = 52 % Initial XCO_2 = 65 % t = 24h	No carbon formation	This work
Ni@CeO_2 (0.25)	Ni embedded into support	GHSV = 43 L.g_{cat}^{-1}.h^{-1} T = 800 °C; P = 1 bar; CH_4/CO_2 = 1.0 Initial XCH_4 = 50 % Initial XCO_2 = 64 % t = 24h	No carbon formation	This work
20Ce/Ni@SiO_2	Ce/Ni coated into SiO_2 nanotubes	GHSV = 36 L.g_{cat}^{-1}.h^{-1} T = 700 °C; P = 1 bar; CH_4/CO_2 = 1.0 Initial XCH_4 = 76 % Initial XCO_2 = 80 % t = 80h	2.2	[51]
Ni/20CeO_2	Multi-layered nanostructured Ni/CeO2	GHSV = 30 L.g_{cat}^{-1}.h^{-1} T = 700 °C; P = 1 bar; CH_4/CO_2 = 1.0 Initial XCH_4 = 85 % Initial XCO_2 = 90 % t = 24h	2.5	[52]
Ni/20CeO_2	Multi-layered nanostructured Ni/CeO2	GHSV = 30 L.g_{cat}^{-1}.h^{-1} T = 700 °C; P = 1 bar; CH_4/CO_2 = 1.0 Initial XCH_4 = 85 % Initial XCO_2 = 90 % t = 24h	19.2	[52]
Ni/CeO_2-S	Ni impregnated over Shuttle-like CeO2	GHSV = 21.6 L.g_{cat}^{-1}.h^{-1} T = 800 °C; P = 1 bar; CH_4/CO_2 = 1.0 Initial XCH_4 = 85 % Initial XCO_2 = 85 % t = 6h	57	[53]
Ni/CeZr(8.5) pH value = 8.5	Ni impregnated over $CeZrO_2$ support prepared by co-precipitation with different pH values	GHSV = 240 L.g_{cat}^{-1}.h^{-1} T = 700 °C; P = 1 bar; CH_4/CO_2 = 1.0 Initial XCH_4 = 78 % Initial XCO_2 = 85 % t = 10h	15	[54]
Ni/$Ce_{0.95}Zr_{0.05}O_2$	Zr-doped CeO_2 nanorods	GHSV = 24 L.g_{cat}^{-1}.h^{-1} T = 800 °C; P = 1 bar; CH_4/CO_2 = 1.0 Initial XCH_4 = 90 % Initial XCO_2 = 94 % t = 100h	No carbon formation	[16]
Ni-PS@$Ce_{0.9}Zr_{0.1}O_2$	Core-shell catalyst structure	GHSV = 18 L.g_{cat}^{-1}.h^{-1} T = 800 °C; P = 1 bar; CH_4/CO_2 = 1.0 Initial XCH_4 = 95 % Initial XCO_2 = 93 % t = 96h	10 wt% weigh loss (No catalyst mass data available)	[47]

Some authors [55–57] have observed the same deactivation behavior at the beginning of the reaction, which has been attributed to the oxidation of metallic Ni particles by CO_2 or H_2O. Rabelo-Neto et al. [13] showed by *in situ* XPS that the surface of metallic Ni particles was oxidized during the DRM reaction when Ni particles were not supported over a reducible oxide. Supporting Ni over $CeSiO_2$ prevented Ni oxidation due to the preferential interaction of CO_2 with oxygen vacancies in the ceria structure. Djinovic et al. [57] studied the performance of $NiCo/Ce_{0.8}Zr_{0.2}O_2$ catalyst for the DRM reaction. The catalyst significantly deactivated during the initial 30 h of TOS, and then, it was observed a slow catalyst regeneration, achieving the initial conversion after 400 h. Concentration profiles of reaction products showed that water yield was the highest at the lowest CH_4 and CO_2 conversions, indicating that RWGS reaction is promoted during catalyst deactivation. Therefore, the authors attributed catalyst deactivation in the initial 25 h of the reaction to the oxidation of NiCo particles by water produced through the RWGS reaction.

In our work, the decrease in Ce/Zr molar ratio limited the ceria reduction and the reactivity of oxygen species on the surface of the support as revealed by isotopic exchange experiments. Therefore, less active sites for CO_2 adsorption are available on the support-metal interface, which might favor the oxidation of Ni nanoparticles. During the reaction, H_2 is partially consumed by the oxidized particles, favoring the *in situ* reduction, which leads to an increase in CH_4 and CO_2 conversion, as observed in Fig. 7 for $Ni@CeZrO_2$ (0.25). Therefore, our catalytic tests suggest the oxidation of Ni nanoparticles over $Ni@CeZrO_2$ (1) and $Ni@CeZrO_2$ (0.25) catalysts; however, further studies must be conducted to analyze the catalyst surface during the reaction.

Furthermore, it has been proposed that the metal crystallite size affects its oxidation kinetics. According to Karmhag et al. [58], smaller particles are more reactive and present a fast oxidation-reduction cycle. Therefore, the embedded catalysts present a decay in activity at the beginning of the reaction followed by reactivation, and an increase in CH_4 and CO_2 conversions can be observed.

As the Ni@CeZrO_2 (4) catalyst exhibited the highest activity and stability among the catalysts studied, it was tested under different reaction conditions. The Ni@CeZrO_2 (4) catalyst was tested at different CH_4/CO_2 molar ratios to study its influence on the conversion and catalyst stability (Fig. 10). When the feed gas is rich in CO_2, a decrease in the CH_4 and CO_2 conversions at the beginning of the reaction is observed. The H_2/CO molar ratio obtained is low, around 0.62, indicating that the excess of CO_2 favors the RWGS reaction [59]. The increase in the CH_4/CO_2 molar ratio leads to an increase in H_2/CO molar ratio, and the catalyst presented better stability. The low availability of CO_2 in the feed gas limits the RWGS reaction, increasing the selectivity to H_2. Then, it seems that the low deactivation observed over time is correlated with the contribution of the RWGS reaction as a side reaction in the DRM process [57].

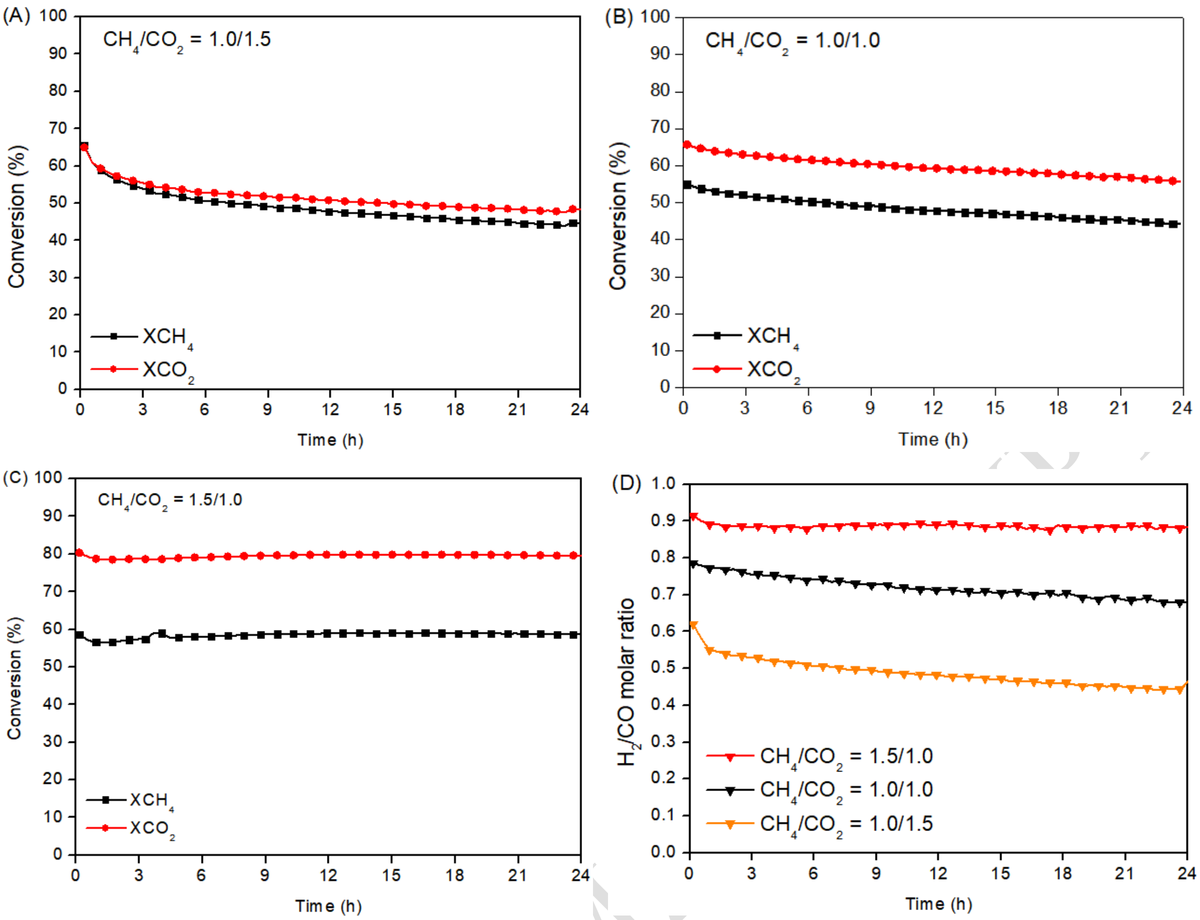

Figure 10. DRM tests over Ni@CeZrO$_2$ (4) catalyst under different feed gas composition as a function of TOS at 800 °C: (A) CH$_4$/CO$_2$ = 0.67; (B) CH$_4$/CO$_2$ = 1.0; (C) CH$_4$/CO$_2$ = 1.5; (D) H$_2$/CO molar ratio.

The TGA (Fig. S3) and DTG (Fig. 8B) curves did not detect the presence of carbon deposits on the Ni@CeZrO$_2$ (4) catalyst for the tests at CH$_4$/CO$_2$ of 0.67 and 1.0. The increase in the CH$_4$/CO$_2$ molar ratio to 1.5 leads to the formation of carbon deposits, as demonstrated by TGA analysis of spent catalyst with a weight loss around 4 wt% (Fig. S2). DTG curve (Fig. 8B) shows a peak at 420 °C ascribed to the oxidation of amorphous carbon and a shoulder at 540 °C correlated to organized carbon structures, such as carbon filaments [60,61]. In this case, the Ni particle is still available for the reagents and no deactivation is observed during the catalytic test (Fig. 10C). Furthermore, a negative peak around 280 °C is observed, associated with the oxidation of Ni^0 particles [62]. Using the TGA curve (Fig. S3), the rate of carbon formation under $CH_4/CO_2 = 1.5$ was calculated: 4.1 mgC g_{cat}^{-1} h^{-1}. Some authors also detected coke deposition produced by methane decomposition when the reaction was performed under $CH_4/CO_2 \geq 1.0$ [63]. It is important to note that the rate of carbon formation in this catalyst is low compared to other works in the literature (Table 4).

Numerous studies in the literature [64–66] have extensively discussed the carbon formation mechanism over Ni-based catalysts during DRM. This mechanism involves the dissociation of methane on the surface of nickel particles, resulting in the production of hydrogen and highly reactive amorphous carbon species (C_α). For a support with redox properties, such as CeO_2 and $CeZrO_2$ mixed oxides, this carbon species can react with oxygen from the support, inhibiting the accumulation of carbon deposits. The oxygen vacancies produced act as active sites for CO_2 dissociative adsorption, which increases the amount of oxygen species on catalyst surface and promotes the gasification of amorphous carbon. Thus, the support plays a crucial role in the DRM reaction, preventing the deposition of carbon on the metal surface.

Ni catalyst supported on Ce-based supports has shown improved stability due to the higher oxygen storage capacity, producing labile lattice oxygen species that contribute to carbon oxidation [67,68]. Recently, Yan et al. [67] studied the performance of Ni/CeO_2-SiO_2 catalyst prepared by dielectric-barrier discharge plasma for DRM at 700 °C. This catalyst contains CeO_2 with more reactive oxygen species in close contact with Ni nanoparticles, which promoted catalyst stability. Smal et al. [68] analyzed the carbon deposition during DRM reaction over $Ni/CeZrO_2$ and $Ni/CeTiZrO_2$ catalysts. It was found that the addition of Ti led to an approximately fourfold decrease in oxygen mobility compared to unmodified $CeZrO_2$. Consequently, no carbon deposits were detected in the $Ni/CeZrO_2$ catalyst after 25h of reaction, while a 2.75wt% weight loss was reported for the $Ni/CeZrTiO_2$ spent catalyst. Then, the optimization of oxygen mobility in the material is fundamental to reach high stability and activity during the DRM reaction.

Another important parameter in the catalyst design for DRM reaction is the Ni particle size, which strongly affects the rate of carbon formation [69]. The initiation step of carbon formation is not favored on small Ni particles, leading to low or absence of coke deposits on catalysts with small Ni particle size. Wang et al. [25] demonstrated that Ni nanoparticles confined within SiO_2 spheres in Ni@SiO_2 catalyst can inhibit metal sintering during DRM reaction, resulting in low carbon formation. Das et al. [47] studied the performance of Ni@$CeZrO_2$ catalyst prepared by ammonia evaporation method with different Ce/Zr molar ratios for the DRM reaction. They obtained the highest oxygen storage capacity for the $Ce_{0.95}Zr_{0.05}O_2$ catalyst, resulting in the absence of coke deposits after 24h of TOS. The combination of small Ni particles and oxygen mobility played a crucial role in designing a carbon-resistant catalyst.

Our research demonstrated that the incorporation of Ni nanoparticles into the $CeZrO_2$ structure prevents metal sintering, as confirmed by *in situ* XRD. By controlling the size of the Ni particles, enhancing metal/support interface, and taking advantage of the high oxygen mobility of the Ni@$CeZrO_2$ catalyst, carbon deposition was suppressed, and the mechanism of carbon removal was promoted. However, the increase in CH_4 percentage in the feed and, consequently, the enhancement of the rate of CH_4 decomposition, results in the enrichment of C_α species over the catalyst surface. The unbalance between the rate of CH_4 decomposition and carbon gasification in the metal/support interface can cause the accumulation of less active carbon species (C_β), which may migrate into the nickel particle, producing carbon filaments [70]. Therefore, carbon deposits were detected in the catalyst after reaction under CH_4/CO_2 molar ratio of 1.5. Considering that the CH_4/CO_2 = 1.5 molar ratio is close to real biogas composition [71], this simulated biogas will be used to evaluate the influence of H_2O addition on the catalyst stability, carbon deposition, and syngas composition.

3.3. DRM reaction: Effect of H_2O addition

The Ni@CeZrO$_2$ (4) catalyst was tested in the DRM reaction in the presence of water, and the CH_4 and CO_2 conversions are displayed in Fig. 11. The water/carbon molar ratio used was 0.4. The addition of water promotes the combined reforming reaction (Eq. 8), occurring at same time the DRM and SRM. The catalyst presented a gradual decrease in the CH_4 and CO_2 conversion values during TOS, with a constant value of the H_2/CO molar ratio around 1.5, lower than the theoretical value of 2.0, since the feed gas is not at stoichiometric conditions. Other authors also reported that the catalyst is initially deactivated under reforming conditions with H_2O [72,73].

$$3\ CH_4 + CO_2 + 2\ H_2O \rightleftharpoons 4\ CO + 8\ H_2 \qquad \Delta H_{298\ K} = 220\ kJ/mol \qquad (8)$$

The post-reaction catalyst was analyzed by TGA (Fig. S3), and the DTG profile is presented in Fig. 8C. It is noticed that the addition of water suppressed the formation of carbon that was observed in the DRM reaction with $CH_4/CO_2 = 1.5$. The presence of steam minimizes and/or suppresses the formation of carbon due to the gasification reaction (Eq. 9). Geng et al. [74] performed a micro-kinetic study to evaluate the water influence in the DRM process, and they observed an enrichment of *OH groups over the catalyst surface promoted by water, reducing the surface coverage of C_α species, well-known as carbon deposit precursors. Therefore, the decrease in conversion observed during the catalytic test is not caused by coke formation.

$$C(s) + H_2O \rightleftharpoons CO + H_2 \tag{9}$$

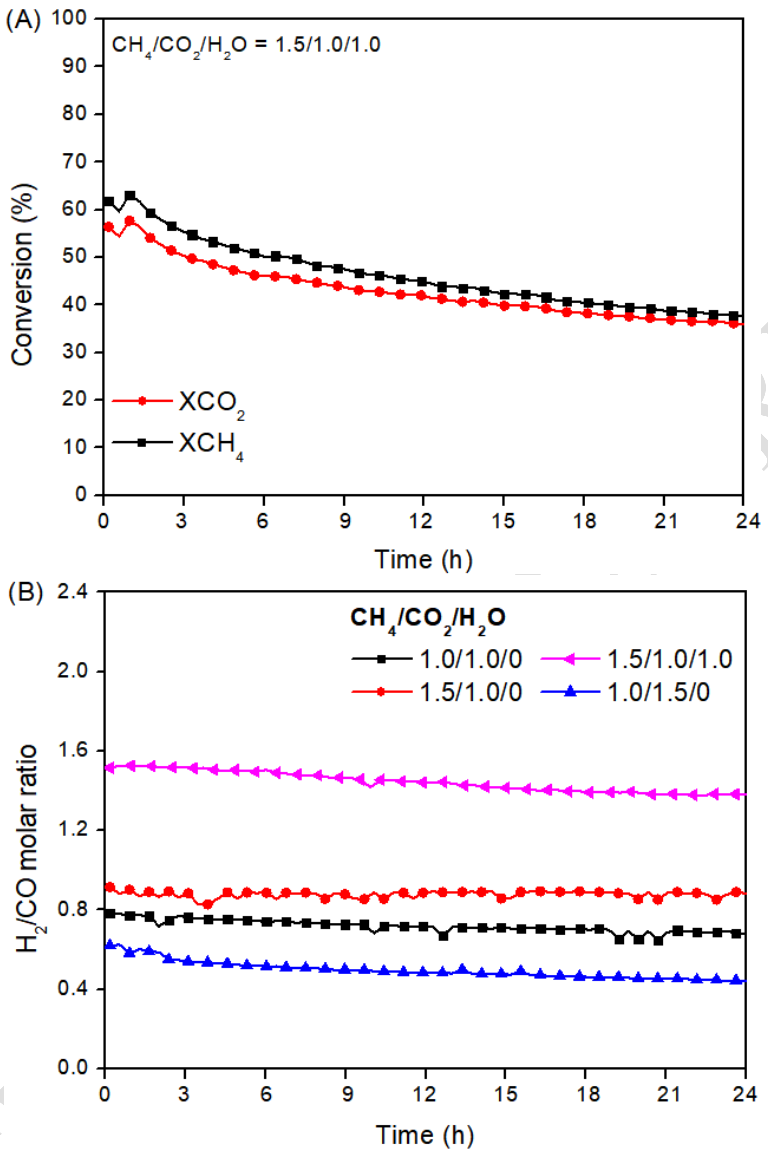

Figure 11. (A) Conversion of CH_4 and CO_2 for the Ni@$CeZrO_2$ (4) catalyst in the combined reforming reaction as a function of TOS at 800 °C; (B) H_2/CO molar ratio obtained in the DRM and SRM reactions as a function of $CH_4/CO_2/H_2O$ molar ratio.

In order to investigate the cause of catalyst deactivation, the catalyst was tested under alternate feed gas composition (Fig. 12). The Ni@$CeZrO_2$ (4) catalyst continuously deactivated during the first 24 h of TOS under a feed gas containing a $CH_4/CO_2/H_2O$ molar ratio of

1.5/1.0/1.0 (step 1). Then, the inlet gas was changed to pure H_2 at 800 °C for 1 h. After treatment under H_2, the reaction was restarted under a feed with the same previous composition (step 2). The CH_4 and CO_2 conversions obtained were higher compared to the initial conversion. This result rules out the hypothesis of Ni sintering under BRM conditions. In our previous work [30], we demonstrated by TEM analysis of the post-reaction sample after DRM reaction that the Ni@CeZrO_2 (4) catalyst has high resistance to the sintering process even after 24 h of TOS.

In step 3, the catalyst was resubmitted to another treatment with H_2, and then it was exposed to a feed containing only CH_4 and CO_2. The conversion values are similar to the ones obtained for the DRM test under CH_4/CO_2 = 1.5/1.0 with the fresh catalyst (Fig. 10c). Therefore, the deactivation observed during BRM is due to a chemical modification of the active phase that is reversible by H_2 treatment, which is likely due to the oxidation of Ni particles by H_2O. The presence of steam provides a higher oxidant power to the reaction medium, promoting the oxidation of coke as well as the metallic Ni particles.

The presence of water in the reactor is still subject to discussion in the literature for DRM and other reactions. Wolf et al. [75] observed that water induces the oxidation and sintering of Co nanoparticles during the Fischer-Tropsch reaction. Liu et al. [76] associated the addition of a small amount of water in the CH_4 feed with the reduction of coke formation in methane dehydroaromatization reaction on Mo/HZSM-5 catalyst. However, the excess of water leads to structural modification in the catalyst, resulting in deactivation.

Djinovic et al. [57] also observed the oxidation of Ni particles by water produced in the RWGS reaction, which occurs simultaneously with the DRM reaction. According to the authors, the Ni oxidation by water is favored at small nanoparticles, and the metal sintering observed during the reaction was favorable to prevent the oxidation after 20 h of reaction. Therefore, in our work, the addition of water to promote the BRM reaction has a double effect:

(i) enhance the rate of coke gasification under high CH_4 content; (ii) increase the Ni oxidation, resulting in a decay of CH_4 and CO_2 conversion with time.

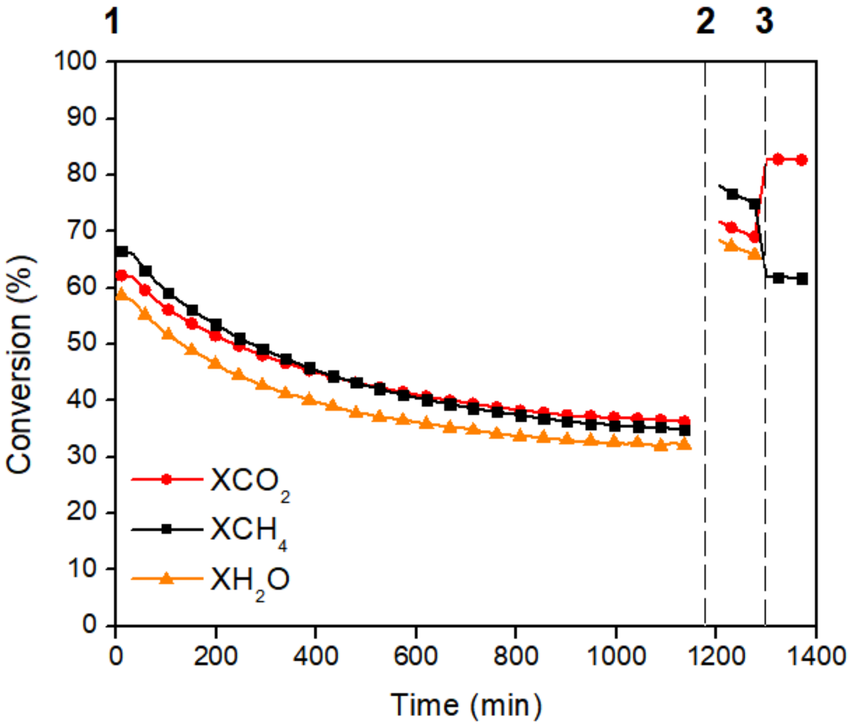

Figure 12. Combined reforming reaction over Ni@CeZrO_2 (4) catalyst by switching the composition of the feed: (1) Reduced catalyst with a feed containing $CH_4/CO_2/H_2O$ = 1.5/1.0/1.0; (2) Treatment with H_2 followed by a feed containing the same composition $CH_4/CO_2/H_2O$ = 1.5/1.0/1.0; (3) Treatment with H_2 followed by stream of CH_4/CO_2 = 1.5/1.0.

4. Conclusions

In our study, we investigated the performance of Ni@CeZrO_2 embedded catalysts with different Ce/Zr molar ratios (4, 1, and 0.25) for the DRM reaction. The catalysts were prepared via the sol-gel method, a rapid and simple one-step synthesis procedure. This method promoted the formation of highly dispersed Ni particles (2-5 nm) embedded in the ceria-zirconia structure even after reduction at high temperature (800°C). The variation of the Ce/Zr molar ratio strongly affected the oxygen mobility of the catalysts. The decrease in the Ce/Zr molar ratio reduced the amount of oxygen mobility and the rate of oxygen exchange because the oxygen atoms linked to Zr are not exchangeable. The Ce/Zr molar ratio also influenced the performance of Ni@CeZrO$_2$ embedded catalysts for DRM under a CH$_4$/CO$_2$ molar ratio of 1.0. The Ni@CeZrO$_2$ (4) catalyst was quite stable whereas Ni@CeZrO$_2$ (1) and Ni@CeZrO$_2$ (0.25) catalysts showed a decrease in the CH$_4$ and CO$_2$ conversions at the beginning of the reaction, followed by reactivation. DTG curves did not show the presence of carbon deposits. The high interaction between Ni and the support created by the embedded structure inhibited Ni sintering and carbon formation, regardless of the Ce/Zr molar ratio. The initial deactivation of Ni@CeZrO$_2$ (1) and Ni@CeZrO$_2$ (0.25) catalysts was attributed to the oxidation of the surface of Ni particles by the CO$_2$ in the feed. Reduced particles were regenerated under the produced syngas, and the CH$_4$ and CO$_2$ conversions returned to the initial values. Further increase in the CH$_4$/CO$_2$ molar ratio to 1.5 caused the formation of coke, which was suppressed by the addition of water. Finally, the Ni@CeZrO$_2$ (4) catalyst showed high catalytic activity and stability due to the strong resistance to Ni sintering and the support assisted in the oxidation of carbon species provided by the embedded structure and optimum Zr content, making it a promising catalyst for the DRM reaction.

5. Acknowledgements

The authors thank CNPq (Conselho Nacional de Desenvolvimento Científico e Tecnológico, Brazil, 308200/2014-7 and 303667/2018-4), CAPES (Coordenação de Aperfeiçoamento de Pessoal de Ensino Superior, Brazil, Finance code 001) and CAPES – COFECUB program (88881.142911/2017-01) for supporting this research and the scholarship received. European Union (ERDF) and Région Nouvelle Aquitaine region are also gratefully acknowledged for their financial support. F. B. Noronha also thanks the French government through the Programme Investissement d’Avenir (I-SITE ULNE/ANR-16-IDEX-0004 ULNE) managed by the Agence Nationale de la Recherche, LIA CNRS France-Brazil “Energy &

Environment", Métropole Européen de Lille (MEL) and Region Hauts-de-France for "CatBioInnov". The group also thanks Sandrine Arii and Nadia Guignard for *in situ* XRD and Raman experiments, respectively.

6. References

[1] Sikiru S, Oladosu TL, Amosa TI, Olutoki JO, Ansari MNM, Abioye KJ, et al. Hydrogen-powered horizons: Transformative technologies in clean energy generation, distribution, and storage for sustainable innovation. Int J Hydrog Energy 2024;56:1152–82. https://doi.org/10.1016/j.ijhydene.2023.12.186.

[2] Sayer M, Ajanovic A, Haas R. Economic and environmental assessment of different hydrogen production and transportation modes. Int J Hydrog Energy 2024;65:626–38. https://doi.org/10.1016/j.ijhydene.2024.04.073.

[3] Vasan V, Sridharan NV, Feroskhan M, Vaithiyanathan S, Subramanian B, Tsai P-C, et al. Biogas production and its utilization in internal combustion engines - A review. Process Saf Environ Prot 2024;186:518–39. https://doi.org/10.1016/j.psep.2024.04.014.

[4] Kumar R, Kumar A. Recent advances of biogas reforming for hydrogen production: Methods, purification, utility and techno-economics analysis. Int J Hydrog Energy 2024. https://doi.org/10.1016/j.ijhydene.2024.02.143.

[5] Song Q, Ran R, Wu X, Si Z, Weng D. Dry reforming of methane over Ni catalysts supported on micro- and mesoporous silica. J CO_2 Util 2023;68:102387. https://doi.org/10.1016/j.jcou.2022.102387.

[6] Kumar R, Kumar A, Pal A. Overview of hydrogen production from biogas reforming: Technological advancement. Int J Hydrog Energy 2022;47:34831–55. https://doi.org/10.1016/j.ijhydene.2022.08.059.

[7] Mortensen PM, Dybkjær I. Industrial scale experience on steam reforming of CO_2-rich gas. Appl Catal Gen 2015;495:141–51. https://doi.org/10.1016/j.apcata.2015.02.022.

[8] Arora S, Prasad R. An overview on dry reforming of methane: strategies to reduce carbonaceous deactivation of catalysts. RSC Adv 2016;6:108668–88. https://doi.org/10.1039/C6RA20450C.

[9] Abdulrasheed A, Jalil AA, Gambo Y, Ibrahim M, Hambali HU, Shahul Hamid MY. A review on catalyst development for dry reforming of methane to syngas: Recent advances. Renew Sustain Energy Rev 2019;108:175–93. https://doi.org/10.1016/j.rser.2019.03.054.

[10] Ponugoti PV, Pathmanathan P, Rapolu J, Gomathi A, Janardhanan VM. On the stability of Ni/γ-Al_2O_3 catalyst and the effect of H_2O and O_2 during biogas reforming. Appl Catal Gen 2023;651:119033. https://doi.org/10.1016/j.apcata.2023.119033.

[11] Stagg-Williams SM, Noronha FB, Fendley G, Resasco DE. CO_2 Reforming of CH_4 over Pt/ZrO_2 Catalysts Promoted with La and Ce Oxides. J Catal 2000;194:240–9. https://doi.org/10.1006/jcat.2000.2939.

[12] Noronha FB, Fendley EC, Soares RR, Alvarez WE, Resasco DE. Correlation between catalytic activity and support reducibility in the CO_2 reforming of methane over Pt/$Ce_xZr_{1-x}O_2$ catalysts. Chem Eng J 2001;82:21–31. https://doi.org/10.1016/S1385-8947(00)00368-5.

[13] Rabelo-Neto RC, Sales HBE, Inocêncio CVM, Varga E, Oszko A, Erdohelyi A, et al. CO_2 reforming of methane over supported $LaNiO_3$ perovskite-type oxides. Appl Catal B Environ 2018;221:349–61. https://doi.org/10.1016/j.apcatb.2017.09.022.

[14] Vasiliades MA, Damaskinos CM, Lykaki M, Stefa S, Binas VD, Kentri T, et al. Deciphering the role of nano-CeO_2 morphology on the dry reforming of methane over Ni/CeO_2 using transient and isotopic techniques. Appl Catal B Environ Energy 2024;350:123906. https://doi.org/10.1016/j.apcatb.2024.123906.

[15] Azevedo IR, da Silva AAA, Xing YT, Rabelo-Neto RC, Luchters NTJ, Fletcher JCQ, et al. Long-term stability of Pt/$Ce_{0.8}Me_{0.2}O_{2-\gamma}$/$Al_2O_3$ (Me = Gd, Nb, Pr, and Zr) catalysts for steam reforming of methane. Int J Hydrog Energy 2022;47:15624–40. https://doi.org/10.1016/j.ijhydene.2022.03.067.

[16] Zou Z, Zhang T, Lv L, Tang W, Zhang G, Gupta RK, et al. Preparing a Zr-Doped CeO_2 Nanorod to Improve the Catalytic Performance of the Ni-Based Catalyst for Dry Reforming of Methane by Enhancing Oxygen Supply. ACS Sustain Chem Eng 2023;11:7443–53. https://doi.org/10.1021/acssuschemeng.3c00419.

[17] Tu PH, Sakamoto M, Sasaki K, Shiratori Y. Synthesis of flowerlike ceria–zirconia solid solution for promoting dry reforming of methane. Int J Hydrog Energy 2022;47:42171–84. https://doi.org/10.1016/j.ijhydene.2021.09.025.

[18] Vogt C, Kranenborg J, Monai M, Weckhuysen BM. Structure Sensitivity in Steam and Dry Methane Reforming over Nickel: Activity and Carbon Formation. ACS Catal 2020;10:1428–38. https://doi.org/10.1021/acscatal.9b04193.

[19] da Fonseca RO, Ponseggi AR, Rabelo-Neto RC, Simões RCC, Mattos LV, Noronha FB. Controlling carbon formation over Ni/CeO_2 catalyst for dry reforming of CH_4 by tuning Ni crystallite size and oxygen vacancies of the support. J CO_2 Util 2022;57:101880. https://doi.org/10.1016/j.jcou.2021.101880.

[20] Bengaard HS, Nørskov JK, Sehested J, Clausen BS, Nielsen LP, Molenbroek AM, et al. Steam Reforming and Graphite Formation on Ni Catalysts. J Catal 2002;209:365–84. https://doi.org/10.1006/jcat.2002.3579.

[21] Chava R, Seriyala AK, Varma D BA, Yeluvu K, Roy B, Appari S. Investigation of Ba doping in A-site deficient perovskite Ni-exsolved catalysts for biogas dry reforming. Int J Hydrog Energy 2023;48:27652–70. https://doi.org/10.1016/j.ijhydene.2023.03.464.

[22] Marinho ALA, Toniolo FS, Noronha FB, Epron F, Duprez D, Bion N. Highly active and stable Ni dispersed on mesoporous CeO_2-Al_2O_3 catalysts for production of syngas by dry reforming of methane. Appl Catal B Environ 2021;281:119459. https://doi.org/10.1016/j.apcatb.2020.119459.

[23] Meng Q, Loughney PA, Joshi A, Sunny AA, Kumar S, Mohapatra P, et al. Enhancing dry reforming of methane with engineered SBA-15-supported Fe-Ni alloy nanoparticles for sustainable syngas production. J CO_2 Util 2024;81:102717. https://doi.org/10.1016/j.jcou.2024.102717.

[24] Zhang J, Li F. Coke-resistant Ni@SiO$_2$ catalyst for dry reforming of methane. Appl Catal B Environ 2015;176–177:513–21. https://doi.org/10.1016/j.apcatb.2015.04.039.

[25] Wang F, Xu L, Shi W. Syngas production from CO$_2$ reforming with methane over core-shell Ni@SiO$_2$ catalysts. J CO$_2$ Util 2016;16:318–27. https://doi.org/10.1016/j.jcou.2016.09.001.

[26] Lim Z-Y, Tu J, Zhou F, Chen B, Choy KL. Unlocking exceptional diffusion of porous Ni@SiO$_2$ nanocapsule catalysts for enhanced dry reforming of methane. Appl Catal B Environ Energy 2024;350:123891. https://doi.org/10.1016/j.apcatb.2024.123891.

[27] Das S, Pérez-Ramírez J, Gong J, Dewangan N, Hidajat K, Gates BC, et al. Core–shell structured catalysts for thermocatalytic, photocatalytic, and electrocatalytic conversion of CO$_2$. Chem Soc Rev 2020;49:2937–3004. https://doi.org/10.1039/C9CS00713J.

[28] Marinho ALA, Rabelo-Neto RC, Epron F, Toniolo FS, Noronha FB, Bion N. Effect of Metal Dopant on the Performance of Ni@CeMeO$_2$ Embedded Catalysts (Me = Gd, Sm and Zr) for Dry Reforming of Methane. Methane 2022;1:300–19. https://doi.org/10.3390/methane1040023.

[29] Marinho ALA, Rabelo-Neto RC, Epron F, Bion N, Noronha FB, Toniolo FS. Pt nanoparticles embedded in CeO$_2$ and CeZrO$_2$ catalysts for biogas upgrading: Investigation on carbon removal mechanism by oxygen isotopic exchange and DRIFTS. J CO$_2$ Util 2021;49:101572. https://doi.org/10.1016/j.jcou.2021.101572.

[30] Marinho ALA, Rabelo-Neto RC, Epron F, Bion N, Toniolo FS, Noronha FB. Embedded Ni nanoparticles in CeZrO$_2$ as stable catalyst for dry reforming of methane. Appl Catal B Environ 2020;268:118387. https://doi.org/10.1016/j.apcatb.2019.118387.

[31] Li R, Zhang J, Shi J, Li K, Liu H, Zhu X. Regulation of metal-support interface of Ni/CeO$_2$ catalyst and the performance of low temperature chemical looping dry reforming of methane. J Fuel Chem Technol 2022;50:1458–70. https://doi.org/10.1016/S1872-5813(22)60032-X.

[32] Deguchi H, Yoshida H, Inagaki T, Horiuchi M. EXAFS study of doped ceria using multiple data set fit. Solid State Ion 2005;176:1817–25. https://doi.org/10.1016/j.ssi.2005.04.043.

[33] Choi T-Y, Kim H-M, Park M-J, Jeong C-H, Jeong D-W. Effect of ZrO_2 on the performance of Co–CeO_2 catalysts for hydrogen production from waste-derived synthesis gas using high-temperature water gas shift reaction. Int J Hydrog Energy 2022;47:14294–303. https://doi.org/10.1016/j.ijhydene.2022.01.235.

[34] Teles CA, de Souza PM, Braga AH, Rabelo-Neto RC, Teran A, Jacobs G, Resasco, DE, Noronha, FB. The role of defect sites and oxophilicity of the support on the phenol hydrodeoxygenation reaction. Appl Catal B Environ 2019;249:292–305. https://doi.org/10.1016/j.apcatb.2019.02.077.

[35] Liu Y, Luo L, Gao Y, Huang W. CeO_2 morphology-dependent NbO_x –CeO_2 interaction, structure and catalytic performance of NbO_x/CeO_2 catalysts in oxidative dehydrogenation of propane. Appl Catal B Environ 2016;197:214–21. https://doi.org/10.1016/J.APCATB.2016.03.011.

[36] Anjaneya KC, Nayaka GP, Manjanna J, Govindaraj G, Ganesha KN. Preparation and characterization of $Ce_{1-x}Gd_xO_{2-\delta}$ (x = 0.1–0.3) as solid electrolyte for intermediate temperature SOFC. J Alloys Compd 2013;578:53–9. https://doi.org/10.1016/J.JALLCOM.2013.05.010.

[37] Bouvier P, Gupta HC, Lucazeau G. Zone center phonon frequencies in tetragonal zirconia: lattice dynamical study and new assignment proposition. J Phys Chem Solids 2001;62:873–9. https://doi.org/10.1016/S0022-3697(00)00243-2.

[38] Aker V, Ayas N. Valorization of microalgae oil via steam reforming for hydrogen-rich gas production over Ni/CeO_2-ZrO_2. Fuel 2024;357:129924. https://doi.org/10.1016/j.fuel.2023.129924.

[39] Bonk A, Remhof A, Maier AC, Trottmann M, Schlupp MVF, Battaglia C, et al. Low-Temperature Reducibility of $M_xCe_{1-x}O_2$ (M = Zr, Hf) under Hydrogen Atmosphere. J Phys Chem C 2015;120:118–25. https://doi.org/10.1021/acs.jpcc.5b10796.

[40] Prasad M, Ray K, Sinhamahapatra A, Sengupta S. Ni/$Ce_xZr_{1-x}O_2$ catalyst prepared via one-step co-precipitation for CO_2 reforming of CH_4 to produce syngas: role of oxygen storage capacity (OSC) and oxygen vacancy formation energy (OVFE). J Mater Sci 2022;57:2839–56. https://doi.org/10.1007/s10853-021-06720-5.

[41] Cauqui MA, Rodríguez-Izquierdo JM. Application of the sol-gel methods to catalyst preparation. J Non-Cryst Solids 1992;147–148:724–38. https://doi.org/10.1016/S0022-3093(05)80707-0.

[42] Esposito S. “Traditional” Sol-Gel Chemistry as a Powerful Tool for the Preparation of Supported Metal and Metal Oxide Catalysts. Materials 2019;12:668. https://doi.org/10.3390/ma12040668.

[43] Madier Y, Descorme C, Le Govic AM, Duprez D. Oxygen Mobility in CeO_2 and $Ce_xZr_{(1-x)}O_2$ Compounds: Study by CO Transient Oxidation and $^{18}O/^{16}O$ Isotopic Exchange. J Phys Chem B 1999;103:10999–1006. https://doi.org/10.1021/jp991270a.

[44] Trovarelli A, Zamar F, Llorca J, Leitenburg C de, Dolcetti G, Kiss JT. Nanophase Fluorite-Structured CeO_2–ZrO_2 Catalysts Prepared by High-Energy Mechanical Milling. J Catal 1997;169:490–502. https://doi.org/10.1006/jcat.1997.1705.

[45] Roh H-S, Potdar HS, Jun K-W, Kim J-W, Oh Y-S. Carbon dioxide reforming of methane over Ni incorporated into Ce–ZrO_2 catalysts. Appl Catal Gen 2004;276:231–9. https://doi.org/10.1016/j.apcata.2004.08.009.

[46] Wang Y, Chan YS, Zhang R, Yan B. Insights into the contribution of oxygen vacancies on CO_2 activation for dry reforming of methane over ceria-based solid solutions. Chem Eng J 2024;481:148360. https://doi.org/10.1016/j.cej.2023.148360.

[47] Das S, Jangam A, Jayaprakash S, Xi S, Hidajat K, Tomishige K, et al. Role of lattice oxygen in methane activation on Ni-phyllosilicate@$Ce_{1-x}Zr_xO_2$ core-shell catalyst for methane dry reforming: Zr doping effect, mechanism, and kinetic study. Appl Catal B Environ 2021;290:119998. https://doi.org/10.1016/j.apcatb.2021.119998.

[48] Makri MM, Vasiliades MA, Petallidou KC, Efstathiou AM. Effect of support composition on the origin and reactivity of carbon formed during dry reforming of methane over 5wt% Ni/$Ce_{1-x}M_xO_{2-\delta}$ ($M=Zr^{4+}$, Pr^{3+}) catalysts. Catal Today 2016;259:150–64. https://doi.org/10.1016/j.cattod.2015.06.010.

[49] Hasani Estalkhi M, Yousefpour M, Kohestani H, Taherian Z. Catalytic evaluation of Ni–3%Sr-/MCM-41 in dry and steam reforming of methane. Int J Hydrog Energy 2024;68:1344–51. https://doi.org/10.1016/j.ijhydene.2024.04.347.

[50] Li Y, Zhang X, Gao S, Guo W, Liu Z, Wu L, et al. Synthesis of the CeO_2 Support with a Honeycomb-Lantern-like Structure and Its Application in Dry Reforming of Methane Based on the Surface Spatial Confinement Strategy. J Phys Chem C 2023;127:1032–48. https://doi.org/10.1021/acs.jpcc.2c07401.

[51] Zhou Q, Fu X, Hui Lim K, Li Z, Liao M, Lu J, et al. Complete confinement of Ce/Ni within SiO_2 nanotube with high oxygen vacancy concentration for CO_2 methane reforming. Fuel 2022;325:124819. https://doi.org/10.1016/j.fuel.2022.124819.

[52] Zhou R, Mohamedali M, Ren Y, Lu Q, Mahinpey N. Facile synthesis of multi-layered nanostructured Ni/CeO_2 catalyst plus in-situ pre-treatment for efficient dry reforming of methane. Appl Catal B Environ 2022;316:121696. https://doi.org/10.1016/j.apcatb.2022.121696.

[53] Gao S, Li Y, Guo W, Ding X, Zheng L, Wu L, et al. Morphology effect of ceria support with hierarchical structure on the catalytic performance for nickel-based catalysts in dry reforming of methane. Mol Catal 2022;533:112766. https://doi.org/10.1016/j.mcat.2022.112766.

[54] Phichairatanaphong O, Donphai W. Role of Cerium–Zirconium Ratio and Chemical Surface Property of CeO_2–ZrO_2 Supported Nickel-Based Catalysts in Dry Reforming Reaction. Top Catal 2023. https://doi.org/10.1007/s11244-023-01834-3.

[55] Faria EC, Neto RCR, Colman RC, Noronha FB. Hydrogen production through CO2 reforming of methane over Ni/$CeZrO_2$/Al_2O_3 catalysts. Catal Today 2014;228:138–44. https://doi.org/10.1016/j.cattod.2013.10.058.

[56] Takanabe K, Nagaoka K, Nariai K, Aika K. Influence of reduction temperature on the catalytic behavior of Co/TiO_2 catalysts for CH_4/CO_2 reforming and its relation with titania bulk crystal structure. J Catal 2005;230:75–85. https://doi.org/10.1016/j.jcat.2004.11.005.

[57] Djinović P, Črnivec IGO, Erjavec B, Pintar A. Details Behind the Self-Regeneration of Supported NiCo/$Ce_{0.8}Zr_{0.2}O_2$ Bimetallic Catalyst in the CH_4–CO_2 Reforming Reaction. ChemCatChem 2014;6:1652–63. https://doi.org/10.1002/cctc.201400059.

[58] Karmhag R, Tesfamichael T, Wäckelgård E, Niklasson GA, Nygren M. Oxidation Kinetics of Nickel Particles: Comparison Between Free Particles and Particles in an Oxide Matrix. Sol Energy 2000;68:329–33. https://doi.org/10.1016/S0038-092X(00)00025-6.

[59] Mosaad Awad M, Kotob E, Ahmed Taialla O, Hussain I, Ganiyu SA, Alhooshani K. Recent developments and current trends on catalytic dry reforming of Methane: Hydrogen Production, thermodynamics analysis, techno feasibility, and machine learning. Energy Convers Manag 2024;304:118252. https://doi.org/10.1016/j.enconman.2024.118252.

[60] Sánchez-Sánchez MC, Navarro RM, Fierro JLG. Ethanol steam reforming over $Ni/M_xO_y–Al_2O_3$ (M=Ce, La, Zr and Mg) catalysts: Influence of support on the hydrogen production. EHEC2005 2007;32:1462–71. https://doi.org/10.1016/j.ijhydene.2006.10.025.

[61] de Lima SM, da Silva AM, da Costa LOO, Assaf JM, Jacobs G, Davis BH, Mattos, LV, Noronha, FB, Evaluation of the performance of Ni/La_2O_3 catalyst prepared from $LaNiO_3$ perovskite-type oxides for the production of hydrogen through steam reforming and oxidative steam reforming of ethanol. Appl Catal Gen 2010;377:181–90. https://doi.org/10.1016/j.apcata.2010.01.036.

[62] Matus E, Sukhova O, Kerzhentsev M, Ismagilov I, Yashnik S, Ushakov V, Stonkus, O, Gerasimov, E, Nikitin, A, Bharali, P, Ismagilov, Z, Hydrogen Production through Bi-Reforming of Methane: Improving Ni Catalyst Performance via an Exsolution Approach. Catalysts 2022;12:1493. https://doi.org/10.3390/catal12121493.

[63] T. Cao AN, Nguyen HH, T. Pham T-P, Pham LKH, Ha Le Phuong D, Nguyen NA, N-Vo, D, Pham, P, Insight into the role of material basicity in the coke formation and performance of Ni/Al_2O_3 catalyst for the simulated- biogas dry reforming. J Energy Inst 2023;108:101252. https://doi.org/10.1016/j.joei.2023.101252.

[64] Bradford MCJ, Vannice MA. CO_2 reforming of CH_4. Catal Rev - Sci Eng 1999. https://doi.org/10.1081/CR-100101948.

[65] Li G, Hao H, Jin P, Wang M, Yu Y, Zhang C. Dry reforming of methane over Ni/Al_2O_3 catalysts: Support morphological effect on the coke resistance. Fuel 2024;362:130855. https://doi.org/10.1016/j.fuel.2024.130855.

[66] Corrente MV, Manfro RL, Souza MMVM. Hydrogen production by biogas reforming using Ni/MgO-Al_2O_3 catalysts. Fuel 2024;368:131561. https://doi.org/10.1016/j.fuel.2024.131561.

[67] Yan X, Hu T, Liu P, Li S, Zhao B, Zhang Q, et al. Highly efficient and stable Ni/CeO_2-SiO_2 catalyst for dry reforming of methane: Effect of interfacial structure of Ni/CeO_2 on SiO_2. Appl Catal B Environ 2019;246:221–31. https://doi.org/10.1016/j.apcatb.2019.01.070.

[68] Smal E, Bespalko Y, Arapova M, Fedorova V, Valeev K, Eremeev N, et al. Carbon Formation during Methane Dry Reforming over Ni-Containing Ceria-Zirconia Catalysts. Nanomaterials 2022;12:3676. https://doi.org/10.3390/nano12203676.

[69] Rostrup-Nielsen JR. Equilibria of decomposition reactions of carbon monoxide and methane over nickel catalysts. J Catal 1972;27:343–56. https://doi.org/10.1016/0021-9517(72)90170-4.

[70] Trimm DL. Coke formation and minimisation during steam reforming reactions. Catal Today 1997;37:233–8. https://doi.org/10.1016/S0920-5861(97)00014-X.

[71] Kapoor R, Ghosh P, Tyagi B, Vijay VK, Vijay V, Thakur IS, et al. Advances in biogas valorization and utilization systems: A comprehensive review. J Clean Prod 2020;273:123052. https://doi.org/10.1016/j.jclepro.2020.123052.

[72] Santos DBL, Noronha FB, Hori CE. Bi-reforming of methane for hydrogen production using $LaNiO_3$/$Ce_xZr_{1-x}O_2$ as precursor material. Int J Hydrog Energy 2020;45:13947–59. https://doi.org/10.1016/j.ijhydene.2020.03.096.

[73] Eltejaei H, Reza Bozorgzadeh H, Towfighi J, Reza Omidkhah M, Rezaei M, Zanganeh R, et al. Methane dry reforming on Ni/$Ce_{0.75}Zr_{0.25}O_2$–$MgAl_2O_4$ and Ni/$Ce_{0.75}Zr_{0.25}O_2$–γ-alumina: Effects of support composition and water addition. Int J Hydrog Energy 2012;37:4107–18. https://doi.org/10.1016/j.ijhydene.2011.11.128.

[74] Geng Z, Gao J, Dong H, Wang S, Zhang M. The role of water in bi-reforming of methane: a micro-kinetic study. React Kinet Mech Catal 2022;135:705–21. https://doi.org/10.1007/s11144-022-02193-y.

[75] Wolf M, Fischer N, Claeys M. Capturing the interconnectivity of water-induced oxidation and sintering of cobalt nanoparticles during the Fischer-Tropsch synthesis in situ. J Catal 2019;374:199–207. https://doi.org/10.1016/j.jcat.2019.04.030.

[76] Liu S, Ohnishi R, Ichikawa M. Promotional role of water added to methane feed on catalytic performance in the methane dehydroaromatization reaction on Mo/HZSM-5 catalyst. J Catal 2003;220:57–65. https://doi.org/10.1016/S0021-9517(03)00236-7.